scientific reports

Check for updates

OPEN

Rational computational design and development of an immunogenic multiepitope vaccine incorporating transmembrane proteins of *Fusobacterium necrophorum*

Muhammad Naveed[1]✉, Muhammad Toheed[1], Tariq Aziz[2]✉, Muhammad Asim[1], Parveen Qadir[1], Hafiz Muzzammel Rehman[3], Rania Ali El Hadi Mohamed[4], Fakhria A. Al-Joufi[5], Maher S. Alwethaynani[6] & Deema Fallatah[7]

Fusobacterium necrophorum **is a Gram-negative, anaerobic pathogen responsible for Lemierre's syndrome, bovine foot rot, and other necrotizing infections. The rise in antimicrobial resistance and the absence of effective vaccines underscore the need for alternative therapeutic strategies. This study employs computational biology to design a multi-epitope vaccine targeting transmembrane proteins of *F. necrophorum* to elicit strong immune responses. The selected proteins were evaluated for toxicity, allergenicity, and antigenicity, followed by epitope prediction and screening. B and T cell epitopes were linked using immunogenic linkers, forming a vaccine construct with a VaxiJen score of 0.7293 and a solubility score of 8.30 in *E. coli*. Structural validation using TrRosetta and Ramachandran plots confirmed 97.4% of residues in favored regions, indicating high stability. Population coverage analysis indicated over 99% global applicability, further enhancing its potential impact. Docking studies revealed strong interactions with immune receptors TLR7 and TLR8. TLR7 formed 12 hydrogen bonds, while TLR8(A) formed 9, and TLR8(B) exhibited the highest interaction, forming 13 hydrogen bonds with the vaccine construct. Molecular dynamics simulations confirmed structural stability and receptor engagement. The RMSD stabilized around 4–5 Å, indicating structural stability of the Vaccine-TLR8(B) complex. The Radius of Gyration remained around 36 Å, showing slight compaction over time, while RMSF peaked at 8–9 Å in flexible regions, with lower fluctuations (1.5–2.5 Å) in stable core regions. Principal component analysis (PCA) identified elastic regions critical for biological activity, and the stable energy levels (-5000 kJ/mol) further confirmed the reliability of the binding. Moreover, the vaccine exhibited high expression levels in *E. coli*, as demonstrated using SnapGene software with the pET-29a(+) vector. The vaccine demonstrated strong binding affinities with immune receptors and predicted activation of both humoral and cellular immune responses, including increased IgM, IgG, and cytokine levels. However, experimental validation is necessary to confirm safety and efficacy, and challenges in vaccine manufacturing and variable immune responses across populations must also be addressed.**

Keywords *Fusobacterium necrophorum*, Lemierre's syndrome, Multiepitope vaccine, Molecular docking, Immune simulations, MD simulations

[1]Department of Biotechnology, Faculty of Science and Technology, University of Central Punjab, Lahore, Pakistan. [2]Laboratory of Animal Health Food Hygiene and Quality, University of Ioannina, Arta, Greece. [3]School of Biochemistry & Biotechnology, University of the Punjab, Lahore, Pakistan. [4]Department of Biology, College of Science, Princess Nourah bint Abdulrahman University, P.O. Box 84428, 11671 Riyadh, Saudi Arabia. [5]Department of Pharmacology, College of Pharmacy, Jouf University, 72341 Aljouf, Saudi Arabia. [6]Department of Clinical Laboratory Sciences, College of Applied Medical Sciences, Shaqra University, Alquwayiyah, Riyadh, Saudi Arabia. [7]Department of Medical Laboratory Sciences, College of Applied Medical Sciences, Prince Sattam Bin Abdulaziz University, 11942 Al-Kharj, Saudi Arabia. ✉email: naveed.quaidian@gmail.com; iwockd@gmail.com;

Fusobacterium necrophorum is a gram-negative, non-spore-forming, obligatory anaerobe bacteria, that inhabits the normal microbiota of the oropharyngeal and gastrointestinal systems in both humans and animals[1]. Because of its commensal characteristics, *F. necrophorum* is a prominent opportunistic pathogen capable of causing severe and potentially fatal health conditions[2]. One of its most well-known diseases caused by *F. necrophorum* in humans is Lemierre's syndrome[3].The bacterium has also been associated with various necrotizing infections, such as hepatic abscesses, soft tissue infections, and periodontal diseases[4]. From a livestock perspective, *Fusobacterium necrophorum* is recognized as the primary etiological agent of bovine foot rot, a disease of significant economic importance in the agricultural sector[5].

The incidence of *F. necrophorum* infections is widespread and varies geographically, impacting both public health and livestock[6]. In North America, Lemierre's syndrome, a severe yet rare infection caused by *F. necrophorum*[7], is estimated to occur in approximately 3 to 6 cases per million annually and primarily affecting young adults[8]. Furthermore, *F. necrophorum* is associated with anaerobic liver abscesses and a significant proportion of periodontal infections[9]. Studies report between 2.9 to 5.0 an incidence of Lemierre's syndrome in Europe ranging from 2.9 to 5.0 cases per million individuals annually between from 2010–13 and 2014–17[10]. The bacterium also contributes to dental and oropharyngeal infections involving anaerobes[11]. Despite a lack of comprehensive data in Asia, rural areas report a notable prevalence of *F. necrophorum* in periodontal diseases, especially among populations with poor oral hygiene[10]. In livestock, the bacterium is a major causative factor of foot rot, affecting 30–80% of cattle herds in the impacted regions[12].Although underreporting is common in Africa, studies conducted in Ethiopia and Kenya indicate that *F. necrophorum* contributes to 25–40% of foot rot cases in cattle and sheep[13]. In Australia and New Zealand, where livestock farming is a key economic sector, *F. necrophorum* is responsible for 40–60% of foot rot cases in sheep and cattle, leading to substantial economic detriment[14]. Similarly, in South America such as Brazil and Argentina report *F. necrophorum* as prevalent pathogen in livestock, being detected in 50% of untreated foot rot cases[15]. The global prevalence of *F. necrophorum* infections highlights its dual effect on human health and agricultural practices, requiring need for effective therapeutic interventions[16].

The available treatments for infections caused by *F. necrophorum* primarily involve using antibiotics, with penicillin, metronidazole, and clindamycin frequently administered[17]. However, the increasing prevalence of antimicrobial resistance among anaerobic bacteria poses a challenging problem[18]. The dependence on surgical interventions, such as abscess drainage, in conjunction with antimicrobial therapy highlights the limited efficacy of current treatments for severe infections[19]. Moreover, the lack of vaccines targeting *F. necrophorum* infections increases antibiotic dependence, further increasing the risk of the emergence of resistance[20]. In the case of livestock, foot rot is treated through a combination of antibiotics and preventive strategies, including foot baths however, these approaches frequently exhibit inadequate long-term effectiveness and sustainability[21]. These therapeutic limitations must be addressed through alternative approaches, including vaccine development, to address *F. necrophorum* infections in human and veterinary medicine[22].

The pathogenesis of *F. necrophorum* is linked to its diverse array of virulence factors, which facilitate its survival, propagation, and evasion of host immune defenses[23]. Major virulence factors involve lipopolysaccharides[24], which stimulate robust inflammatory responses, hemolysins, which contribute to tissue damage and leukotoxins, which help in immune evasion. Another crucial factor is adhesins, which facilitate the bacterium's attachment to host tissues, enhancing colonization and persistence[25]. Additionally, the *F. necrophorum* produces hydrogen sulfide and butyric acid which promotes tissue necrosis and creates anaerobic conditions for its growth[26]. The bacterium's ability to establish biofilms confers protection against immune clearance and antimicrobial therapy, complicating the management of infections[27].

This research aims to utilize computational biology for the in-silico design of a multiepitope vaccine by using the transmembrane proteins of *F. necrophorum*. Transmembrane proteins present promising targets for vaccination due to their accessibility to the immune system and their involvement in bacterial adhesion, invasion, and virulence[28]. By implementing computational methods that integrate immunoinformatic methodologies, this study aims to identify and evaluate immunogenic epitopes capable of inducing robust and protective immune responses[29]. The primary objective is to develop a vaccine that not only alleviates the impact of *F. necrophorum* infections but also reduces reliance on antibiotics, thereby addressing the global issue of antimicrobial resistance. This research holds significant potential for enhancing our understanding of *F. necrophorum* pathogenesis and providing novel strategies for its prevention and management.

Methodology

Protein selection and retrieval

The FASTA sequences of target proteins of *F. necrophorum* were retrieved from the UniProt database (https://www.uniprot.org/). The selected proteins include outer membrane efflux protein, translocase subunit SecA, ATP-dependent zinc metalloprotease FtsH, and Protein-export membrane protein SecF having UniProt IDs-A0A0B4EIV6, A0AAI8M1U4, A0AAI8M1J4, , A0A4Q2L0D4, and respectively. These proteins were chosen based on their high antigenicity scores (>0.4), non-allergenicity and non-toxicity, along with their functional roles in bacterial virulence, including adhesion, invasion, and biofilm formation. Their subcellular localization was confirmed using the TMHMM server (https://services.healthtech.dtu.dk/services/TMHMM-2.0/). To identify the antigenic characteristics of the viral protein, we utilized the Vaxijen 2.0 web server (https://www.ddg-pharmfac.net/vaxijen/VaxiJen/VaxiJen.html). The AllerTOP 2.0 server (https://www.ddg-pharmfac.net/allertop_test/) was used to predict protein allergenicity. The toxicity of target proteins was predicted by using the Toxipred server (https://webs.iiitd.edu.in/oscadd/toxipred/supple.php)[30].

Epitopes prediction

The IEDB Bepipred 2.0 available at (http://tools.iedb.org/bcell/) tool was utilized for B-cell epitope prediction (Fig. 1), which relies on a hidden Markov model (HMM) and surface accessibility scores to identify potential B-cell epitopes[31]. The selection cutoff threshold was based on the score threshold 0.5, which Bepipred recommended[32]. Epitopes scoring above this threshold were considered highly probable B-cell epitopes, ensuring strong antigenicity and accessibility for immune recognition. The MHC-I epitope prediction was performed using the Artificial Neural Network (ANN 4.0) algorithm on the IEDB server (http://tools.iedb.org/mhci/), which calculates IC50 binding affinity scores[33]. Only epitopes with IC50 values < 100 nM and percentile ranks < 1% were selected, ensuring high-affinity binding to MHC-I molecules. The MHC-II epitope prediction was conducted using the NN-align algorithm from IEDB server (http://tools.iedb.org/mhcii/) which integrates position-specific scoring matrices (PSSM) and machine-learning techniques[34]. The cut-off for selection was based on IC50 values < 100 nM and a low percentile rank, ensuring strong interactions with MHC-II molecules.

Epitopes screening and evaluation

The final epitopes selection was based on antigenicity, allergenicity, and toxicity analysis. Antigenicity was predicted using the VaxiJen 2.0 server (http://www.ddg-pharmfac.net/Vaxijen/VaxiJen/VaxiJen.html). Allergenicity was assessed using Allertop 2.0 (http://www.ddg-pharmfac.net/AllerTOP), while toxicity was predicted by Toxipred server (https://crdd.osdd.net/oscadd/toxipred/)[35].

Population coverage analysis

The IEDB server (https://www.iedb.org/) was used to evaluate the population coverage of MHC Class I and Class II molecules. For this analysis, the epitopes for each class were first separated into individual Notepad files and then uploaded one by one to IEDB for population coverage assessment[36] . The analysis focused on alleles with high global prevalence, including HLA-A*02:01, HLA-B*07:02, and HLA-DRB1*01:01.

Vaccine construction

The linkers GPGPG, KK, AAY, and AYY were used to join the selected epitopes in the final vaccine construct, optimizing immunogenicity and enhancing epitopes presentation. In the vaccine construct, the MHC-II epitopes, MHC-I epitopes and B-cell epitopes were linked by distinct linkers including GPGPG, KK, AAY, and AYY. GPGPG linker was used to separate different immune epitopes, ensuring proper structural integrity and enhancing antigen processing[37]. The KK (Lys-Lys) linker was used to join the two B cell epitopes because it facilitates B cell receptor recognition which enhances humoral immune response[38]. The AAY and AYY linkers were used for the MHC class I and class II epitopes, respectively, as they are optimal for proteasomal cleavage and subsequent presentation of the epitopes to CD8 + and CD4 + T cells[39].Additionally, a beta-defensin adjuvant

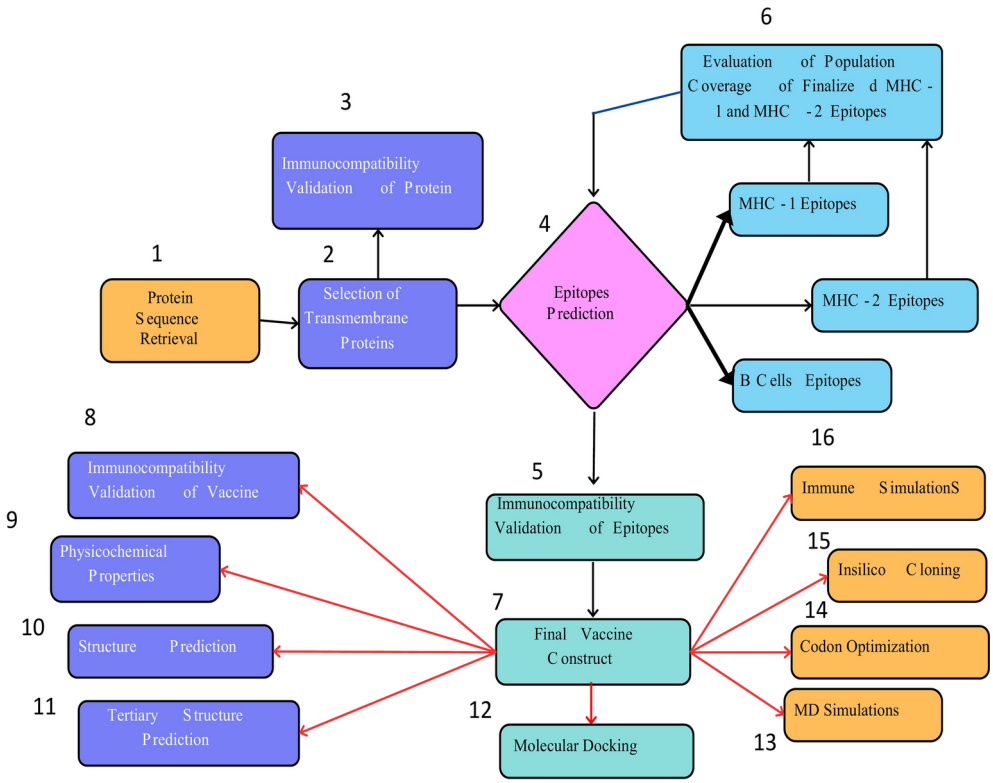

Fig.1. Vaccine Construction against *Fusobacterium necrophorum* Methodology.

was incorporated at the N terminus of the construct to enhance immune simulation and a Padre sequence and 6X Histidine tag was added at the N terminus of the construct to facilitate purification and expression[40].

Physiochemical analysis

The ExPASy ProtParam tool (https://web.expasy.org/protparam/) was utilized for the physicochemical analysis of the vaccine construct. This analysis included determining the theoretical value of the isoelectric point (PI), index of instability, the composition of amino acids, molecular weight, in vivo and in vitro stability, aliphatic index, and GRAVY[41].

Two-dimension structure analysis

For 2D protein structure analysis, the PSIPRED tool (https://bio.tools/psipred) and the GOR IV tool (https://npsa-pbil.ibcp.fr/cgi-bin/secpred_gor4.pl) were used. These tools predict the coil structure, alpha-helix, and beta-sheet of the vaccine construct. PsiPred provides a confidence score for each amino acid indicating the reliability of the secondary structure. A higher the confidence score, the higher the prediction[42].

Three-dimension analysis

TrRosetta (https://yanglab.qd.sdu.edu.cn/trRosetta/) was used to predict the 3D structure of the designed vaccine construct. This tool built the protein structure on direct minimization with restrain Rosetta (Fig. 1). The protein 3D structure was validated by using the Ramachandran plot (https://saves.mbi.ucla.edu/) and the Errat program (https://www.doe-mbi.ucla.edu/errat/) of the Procheck server to evaluate the overall quality of the[43].

Prediction of discontinuous B-Cell Epitopes

The discontinuous B-cell epitopes from the vaccine construct were predicted using Ellipro epitopes, available on IEDB server (http://tools.iedb.org/ellipro/). The vaccine's 3D structure was provided in PDB format, and the system's default parameters, which include a minimum score value of 0.5 and a protrusion index (PI) of 0.7, were selected. Ellipro uses solvent accessibility and structural outline to predict discontinuous epitopes[29].

Disulphide engineering

The disulfide Engineering was performed by using Disulfide by Design 2.0 (DbD2.0) (http://cptweb.cpt.wayne.edu/DbD2/) to increase the stability of the vaccine construct. The vaccine's 3D structure (PDB format) was processed, and the tool was adjusted to scan for possible residue pairs that could associate with disulfide bonds. The selection criteria were the Cα-Cα distance (4.4–6.8 Å), χ3 dihedral angle (±90° or ± 120°), and B-factor stability (< 30 $Å^2$). The corresponding disulfide residue pairs were computationally mutated to cysteine, followed by energy minimization to check the stability of the bonds[44].

Molecular docking and interaction analysis

The molecular docking was performed using the ClusPro server (https://cluspro.org/tut_dock.php), which employs a fast Fourier transform (FFT) correlation approach for rigid-body docking[45]. The server uses a scoring function based on electrostatic and desolvation energies to rank the docked complexes[46]. TLR3, TLR4, TLR7, and TLR8 were chosen due to their well-documented roles in recognizing bacterial components and activating innate immune responses[47]. Toll-like receptors (TLRs) are key receptors in pathogen recognition, triggering downstream signaling pathways that activate both innate and adaptive immunity[48]. TLR3 recognizes double-stranded RNA, which can be relevant in bacterial infections that trigger immune responses through host–pathogen interactions[49]. TLR4 is a major sensor of lipopolysaccharides[24], a crucial virulence factor in Gram-negative bacteria[50]. Meanwhile, TLR7 and TLR8 detect single-stranded RNA and bacterial nucleic acids, playing significant roles in bacterial and viral immunity[51]. These receptors were chosen because they are widely implicated in bacterial immune recognition, particularly against Gram-negative bacteria. Thirty docking runs were performed for each receptor (TLR-3, TLR-4, TLR-7, and TLR-8), and the top-ranked model with the lowest binding energy was selected for further analysis. The selected docked complexes were subjected to molecular dynamics (MD) simulations to assess stability and interactions. Ligplot + v.2.2 (https://www.ebi.ac.uk/thornton-sr v/software/LigPlus/) was used for interaction analysis of the docked complexes[52].

Immune simulation

To conduct immune simulations of the vaccine, the C-IMMSIM server (https://wwwold.iac.rm.cnr.it/~filippo/projects/c-immsim-online.html) was used to predict the immune response activation by the designed vaccine construct. It was used to assess the activation of hormonal, C-cell mediated, and innate immunological response following vaccination. The simulation assessed how epitopes interact with immune receptors such as T-cell and B-cell receptors, leading to the initiation and progression of an immune response[53].

Insilco cloning and codon optimization

The amino acid of the vaccine construct was reverse-translated into nucleotide sequence using EMBOSS Backtranseq tool (https://www.ebi.ac.uk/jdispatcher/st/emboss_backtranseq). Consequently, the codon optimization was performed using the Codon Optimization Tool (ExpOptimizer) (http://novoprolabs.com/tools/codon-optimization/) to enhance vaccine expression efficiency. This tool optimize the codon usage to match the host organism's preference, improving the likelihood of successful expression in a heterologous system[54].To further validate the translational efficiency, we have used RNAfold server to analyze potential mRNA folding that is available at (http://rna.tbi.univie.ac.at/cgi-bin/RNAWebSuite/RNAfold.cgi)[55] . For Insilico cloning SnapGene8.0.0 software was used and the optimized vaccine sequence was inserted into the vector pET29a(+) and cloned[56].

Molecular dynamics simulations

To analyze the conformational changes and stabilities of the vaccine-TLR8 complex, molecular dynamics (MD) simulations were performed with the Desmond from DE Sha Research. Protein Preparation Wizard was used to ensure bond orders and add hydrogen atoms, disulfide, and hydrogen bonds to prepare the system[57]. A 10 Å × 10 Å × 10 Å SPC water model solvation box was created using the System Builder tool. To reduce physiological changes, 0.15 M NaCl and extra Na^+ and Cl^- ions were added for charge balance. Potential energy was minimized using the NPT ensemble method to maintain system stability. MD simulations were performed at a temperature of 300 K and pressure of 1 atm for a duration of 500 ns with the OPLS4 force field, using NPT methodology for OPLS4 production. Before simulation, the system was relaxed, and short-range electrostatic interactions were calculated with the particle mesh Ewald method with a cutoff radius of 9.0 Å[58]. Pressure control was done with the Martyna-Tuckerman-Klein chain coupling scheme (coupling constant = 2.0 ps)3., while the Nosé-Hoover chain coupling scheme was employed for temperature control. The complexes were analyzed using root mean square deviation (RMSD) to examine the stability, and the system also calculated root mean square fluctuation (RMSF) to assess flexibility. The radius of gyration (Rg) was computed using GROMACS after converting the trajectory to XTC format with MDTraj. The calculation was done with the gmx gyrate command[59].

Principal component analysis

PCA is a widely used method for analyzing molecular dynamics (MD) simulation trajectories by transforming high-dimensional data (3N dimensions, where N represents the number of atoms of interest) into a lower-dimensional coordinate system. This dimensionality reduction is achieved by mapping the C-alpha atom coordinates in each frame onto a set of orthogonal vectors known as principal components (PCs). The process begins with computing a covariance matrix of the atomic coordinates, followed by its diagonalization to extract eigenvectors and eigenvalues, from which the principal components are derived[60]. For this study, PCA was performed on GROMACS after the Desmond trajectory was transformed to XTC format with MDTraj[61]. The gmx covar command was used to compute and diagonalize the covariance matrix, generating the principal components based on the protein–protein trajectory. Subsequently, the gmx anaeig command, with the -proj parameter, was utilized to determine the projection of the trajectory onto the principal components, allowing the evaluation of conformational changes[62].

MM/PBSA analysis

The MM/GBSA method was used to calculate the binding free energy of vaccine-TLR8 during MD simulations and calculated using g_mmpbsa[63]. In order to enable analysis, the Desmond simulation trajectories were exported to the PDB format with the receptor and vaccine protein structures . Each frame (PDB file) was handled with CHAPERONg a GROMACS-based tool, and the necessary TPR and XTC files were produced by executing a short molecular dynamics (MD) simulation and then correcting the resultant periodic boundary conditions (PBCs). For the MM/PBSA calculations during the g_mmpbsa calculation, the initial frame of the brief simulation was used[64].

Dynamic Cross-Correlation matrix (DCCM) analysis

The movements of a protein residue may be correlated or anti-correlated to other residues, making it possible to form a dynamic cross-correlation network that includes local and global conformational changes, including protein binding effects[65]. DCCM examines these networks through the correlation of residues with respect to their C-alpha atoms. For any two C-alpha atoms (i, j) there exists a cross-correlation coefficient C(i,j) defined as follows:

$$C(\rangle, j) = \frac{< \mathbf{\Delta r}_{\rangle} . \mathbf{\Delta r}_{j} >}{< \left|\mathbf{\Delta r}_{\rangle}\right|^{2} >^{\frac{1}{2}} < \left|\mathbf{\Delta r}_{j}\right|^{2} >^{\frac{1}{2}}}$$

In this equation, where $\mathbf{\Delta r}_{\rangle}$ represents atomic displacement, and angle brackets denote average values over the simulation path. C(i,j) > 0 corresponds to positive correlation C(i,j) < 0 corresponds to anti-correlated movements while C(i,j) = 0 represents no correlation[66].

In this study, DCCM calculations were performed with Bio3D after Desmond trajectory conversion to DCD format using MDTraj[61].

Analysis of free energy landscape

The Free Energy Landscape[67] examines energy fluctuations during MD simulations based on principal components (PCs) derived from PCA. This method helps identify the metastable conformations of the protein and its energy state. The analysis is based on calculations of Gibbs free energy. For this Analysis, GROMACS was used to analyze FEL using the command gmx sham, which calculated the Gibbs free energy in terms of PC1 and PC2[68]. To improve the visualization, FEL smoothing via Locally Estimated Scatterplot Smoothing regression was performed, and the results were confirmed using Kernel Density Estimation plots from PCA data[57].

Results

Extraction of fusobacterium necrophorum proteins

Approximately 15,778 proteins of *Fusobacterium necrophorum* are available in the UniProt database. From a total of 2722, four transmembrane proteins were selected based on their antigenicity and biological significance. These selected proteins include Protein translocase subunit SecA, ATP-dependent zinc metalloprotease FtsH,

No	UniProt ID	Protein names	Antigenicity	Allergenicity	Toxicity	Functions of proteins
1	A0AAI8M1J4	ATP-dependent zinc metalloprotease FtsH	0.5965	Non-Allergen	Non-Toxic	Acts as a processive, ATP-dependent zinc metallopeptidase for both cytoplasmic and membrane protein
2	A0AAI8M1U4	Protein translocase subunit SecA	0.4919	Non-Allergen	Non-Toxic	Interacts with the SecYEG preprotein conducting channel. Has a central role in coupling the hydrolysis of ATP to the transfer of proteins into and across the cell membrane, serving as an ATP-driven molecular motor driving the stepwise translocation of polypeptide chains across the membrane
3	A0A4Q2L0D4	Protein-export membrane protein SecF	0.5506	Non-Allergen	Non-Toxic	Part of the Sec protein translocase complex. Interacts with the SecYEG preprotein conducting channel. SecDF uses the proton motive force (PMF) to complete protein translocation after the ATP-dependent function of SecA
4	A0A0B4EIV6	Outer membrane efflux protein Outer membrane efflux protein	0.6239	Non-Allergen	Non-Toxic	It facilitates the transport of substances out of the cell and contribute to antibiotic resistance and virulence

Table 1. List of selected transmembrane pathogenic proteins.

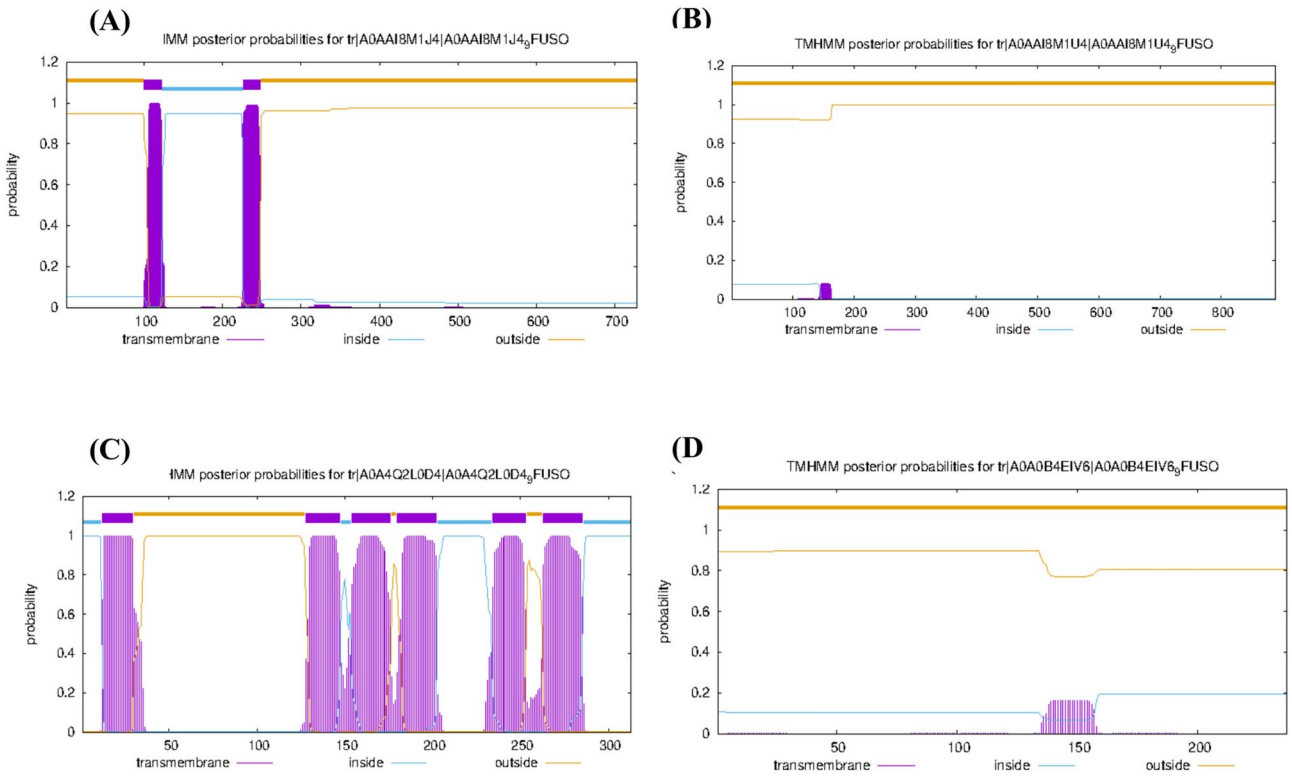

Fig. 2. Graphical representation of Subcellular Locations of all 4 proteins predicted by TMHMM server **(A)** ATP-dependent zinc metalloprotease FtsH **(B)** Protein translocase subunit SecA **(C)** Protein-export membrane protein SecF **(D)** Outer membrane efflux protein Outer membrane efflux protein.

Outer membrane efflux protein, and Protein-export membrane protein SecF, as shown in Table 1. The TMHMM server was used to determine their subcellular localization and the immune compatibility of the selected transmembrane proteins was checked using Allertop, Toxipred, and VaxiJen. Proteins that were non-toxic, non-allergenic and exhibited an antigenic score above 0.4, were chosen for vaccine designing. The subcellular locations are shown in Fig. 2, and additional characteristics are presented in Table 1. These proteins were further analyzed to design a vaccine utilizing multiple epitope vaccine targeting *F. necrophorum*.

Anticipation of B-cell epitope

Four transmembrane proteins for B cell epitopes were retrieved from the IEBD website. Upon antigen binding to host receptors, B cells play a pivotal role in generating B memory cells, which subsequently produce antibodies to opsonize the antigen and help in preventing secondary infections. The predicted epitopes were chosen based on nonallergenic, non-toxic and their antigenicity score, surpassing the predefined criterion of > 0.4 as specified by VaxiJen. The estimates of the selected B-cell epitopes utilized in the vaccine development process are shown in Table 2.

Protein Name	Epitopes	Start	End	Antigenicity	Allergenicity	Toxicity
ATP-dependent zinc metalloprotease FtsH	NKKFSKDV	467	474	0.6108	Non-Allergen	Non-Toxic
Protein translocase subunit SecA	RMYQKLSGMTGTAETEAT	387	404	1.0028	Non-Allergen	Non-Toxic
Protein-export membrane protein SecF	KGLNYGIDFS	30	39	0.9084	Non-Allergen	Non-Toxic
Outer membrane efflux protein Outer membrane efflux protein	IQLKASLKSAEQ	196	207	1.07	Non-Allergen	Non-Toxic

Table 2. Selected B-cell epitopes within target proteins.

Protein Name	Epitopes	Antigenicity	Allergenicity	Toxicity	Alleles	IC50 Score	Rank
ATP-dependent zinc metalloprotease FtsH	FILNLLASW	0.7505	Non-Allergen	Non-Toxic	HLA-B*53:01 HLA-B*58:01	68.51	0.08
	FLLLIFIVA	2.6912	Non-Allergen	Non-Toxic	HLA-A*02:01	69.98	0.64
Protein translocase subunit SecA	ATRDREMMGR	0.8379	Non-Allergen	Non-Toxic	HLA-A*31:01	47.08	0.51
	DILVEAFATV	0.5740	Non-Allergen	Non-Toxic	HLA-A*02:03 HLA-A*02:06 HLA-A*02:01	25.31	0.43
Protein-export membrane protein SecF	FAIGAIIAL	0.5179	Non-Allergen	Non-Toxic	HLA-A*02:06 HLA-B*35:01 HLA-A*68:02 HLA-A*02:01	8.71	0.08
	IIIYITFRF	2.2595	Non-Allergen	Non-Toxic	HLA-A*32:01 HLA-A*23:01	49.71	0.06
Outer membrane efflux protein Outer membrane efflux protein	ISIQVIQQY	0.7183	Non-Allergen	Non-Toxic	HLA-B*58:01 HLA-B*15:01	10.87	0.05
	KIAFGNFLPR	0.7159	Non-Allergen	Non-Toxic	HLA-A*31:01 HLA-A*11:01 HLA-A*68:01	25.21	0.27

Table 3. List of Selected MHC-I Epitopes of Targeted Proteins.

Anticipation of epitopes of MHC Class-I

MHC I class molecules play a vital part in adaptive immunity, contributing to the development of acquired immunity against infections and diseases. To enhance the immune response, MHC class I epitopes are essential in vaccine design. In this study, four transmembrane proteins were analyzed for MHC Class I epitopes, with two epitopes selected from each protein based on their low percentage rank with their corresponding IC50 values, specifically those less than 100. The selected MHC Class I epitopes and their respective characteristics are summarized in Table 3**.**

Prediction of MHC Class-II epitopes

MHC Class II molecule are crucial for acquired immunity and play significant role in pathogen elimination, making their selection crucial for designing subunit vaccines. In this study, Epitopes derived from four different transmembrane proteins were selected, and the relevant alleles were chosen to support the analysis of population coverage. The chosen epitopes were based on the antigenicity score exceeding 0.4 and an evaluation of their non-allergenic properties. It was verified that these selected epitopes are non-toxic and do not provoke allergies. Moreover, the epitopes with the lowest rank and an IC50 value of less than 100 were given priority. The selected epitopes of MHC class II are being given in Table 4.

Population coverage analysis

Using the IEDB server, the anticipated population coverage for both MHC Class-I and Class-II epitopes was evaluated. The analysis yielded a global value of 99.39% indicating the broad potential of the selected epitopes to elicit an immune response across diverse populations. The graph presenting world population coverage is shown in Fig. 3.

The collective MHC Class-I and MHC Class-II epitopes showed the highest level of population coverage (99.99%) in North America, North Africa (97.95%), Europe (99.97%), East Africa (98.59%), East Asia (95.55%), West Africa (96.66%), Central Africa (99.21%), Northeast Asia (97.95%), Southwest Asia (97.89%), Oceania (96.92%), West Indies (90.26%) as shown in Figure 4.

Vaccine construction

Utilizing various immune informatics tools, all predicted epitopes were linked using specific to assemble the final vaccine construct. Eight MHC Class-I epitopes were linked using KK, eight MHC Class-II were connected via AAY and four B cell epitopes were joined using AYY linkers to design the final vaccine construct.

To enhance immunogenicity, an aggregation-promoting peptide, specifically a beta defensin protein sequence was added to the N-terminal N using a GPGPG linker. In order to increase the expression of the vaccine in *E. coli*, a 6X Histidine tag was incorporated at the C-terminus of the vaccine. The Final vaccine construct consists of 353 amino acid sequence in Fig. 5 and Fig. 6.

Protein Name	Epitopes	Antigenicity	Allergenicity	Toxicity	Alleles	IC50 Score	Rank	Start	End
ATP-dependent zinc metalloprotease FtsH	EREGYLYGYSSSEKG	0.6791	Non-Allergen	Non-Toxic	HLA-DRB1*09:01	76.5	7.5	157	171
	FDRQVYVDKPDLKGR	1.1849	Non-Allergen	Non-Toxic	HLA-DRB1*03:01	88	3.8	443	457
Protein translocase subunit SecA	EFVHTYGLEVVVIPT	0.7676	Non-Allergen	Non-Toxic	HLA-DRB1*07:01 HLA-DRB1*01:01 HLA-DRB1*09:01 HLA-DPA1*03:01 HLA-DPB1*04:02	7.6	0.46	405	419
	EIVAQAGRKNSVTIA	0.7649	Non-Allergen	Non-Toxic	HLA-DRB5*01:01 HLA-DRB1*01:01 HLA-DRB1*11:01	88.4	12	494	508
Protein-export membrane protein SecF	DRIRENLKRRGKTDM	0.6334	Non-Allergen	Non-Toxic	HLA-DRB1*11:01	26.6	2.7	203	217
	FAKGLNYGIDFSGGN	0.9441	Non-Allergen	Non-Toxic	HLA-DRB1*07:01	69.5	8.2	28	42
Outer membrane efflux protein Outer membrane efflux protein	KQKWSFFLCLLFLSS	1.5022	Non-Allergen	Non-Toxic	HLA-DPA1*01:03 HLA-DPB1*02:01 HLA-DPA1*01:03 HLA-DPB1*04:01	22.6	0.42	2	16
	KSYSVYGLQASMPIF	0.8586	Non-Allergen	Non-Toxic	HLA-DRB1*01:01 HLA-DRB1*09:01 HLA-DRB1*07:01 HLA-DRB1*04:01 HLA-DRB1*15:01 HLA-DRB5*01:01	10	2.7	134	148

Table 4. List of Selected MHC-II Epitopes of Targeted Proteins.

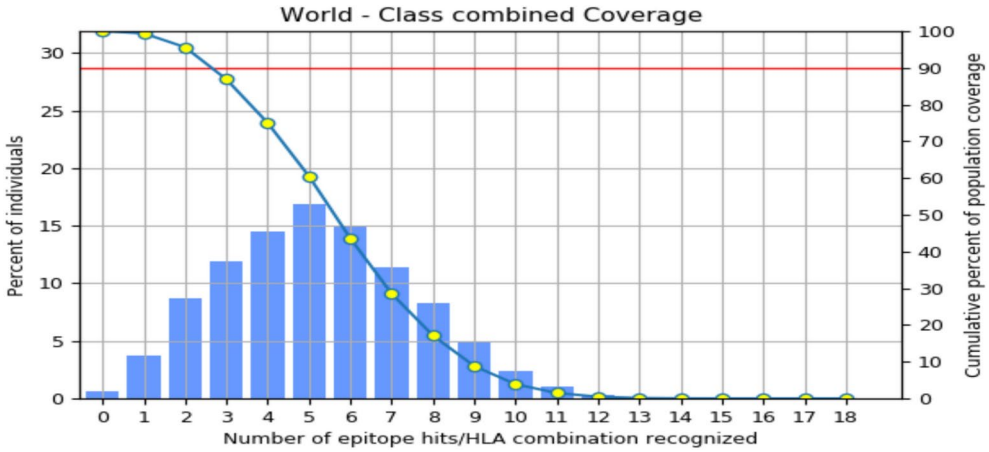

Fig. 3. Global population coverage graph of combined MHC-I and MHC-II epitopes, using IEDB tool.

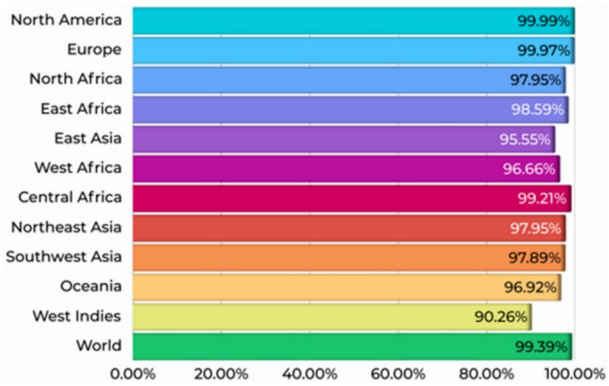

Fig. 4. The combined MHC Class-I and MHC Class-II epitopes population coverage demonstration in different regions of world.

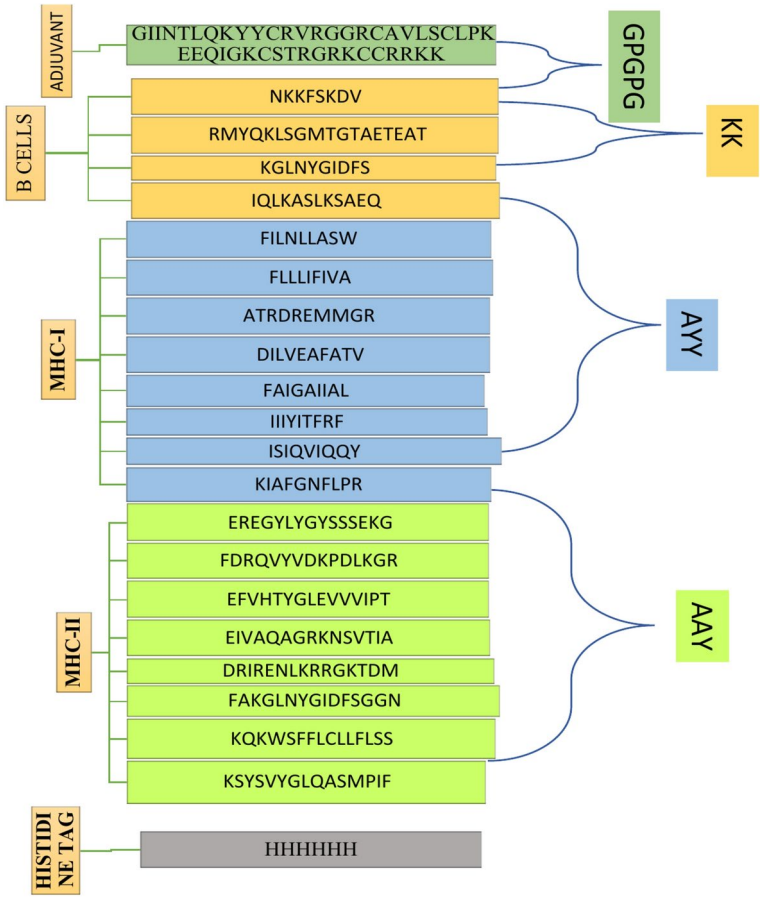

Fig. 5. Schematic diagram of designed vaccine construct.

GIINTLQKYYCRVRGGRCAVLSCLPKEEQIGKCSTRGRKCCRRKKGPGPGNKKFSKDVKKRMYQ
KLSGMTGTAETEATKKKGLNYGIDFSKKIQLKASLKSAEQAAYFILNLLASWAAYFLLLIFIVAAA
YATRDREMMGRAAYDILVEAFATVAAYFAIGAIIALAAYIIIYITFRFAAYISIQVIQQYAAYKIAFGN
FLPRAYYEREGYLYGYSSSEKGAYYFDRQVYVDKPDLKGRAYYEFVHTYGLEVVVIPTAYYEIVA
QAGRKNSVTIAAYYDRIRENLKRRGKTDMAYYFAKGLNYGIDFSGGNAYYKQKWSFFLCLLFLS
SAYYKSYSVYGLQASMPIFHHHHHH

Fig. 6. Designed multiepitope vaccine sequence of vaccine.

Allergenic and antigenic properties anticipation of vaccine

The design vaccine was categorized as non-allergen evaluated using AllerTOP server. The antigenicity was 0.7293, which is greater than the threshold level of 0.4 as predicted by VaxiJen server. Additionally, Toxipred server confirmed that the vaccine construct is non-toxic**.**

Physicochemical properties

The physicochemical characteristics of the multi-epitope vaccine were evaluated using the ExPASy ProtParam server. The findings revealed that the vaccine construct possesses a theoretical isoelectric point (pI) of 9.63 and a molecular weight of 40,307.71 Da. Following this, the stability index was computed and determined to be 23.71, which signifies the stability of the vaccine. The half-life of the designed vaccine was predicted to be over twenty hours in yeast, thirty hours in human mammalian reticulocytes, and more than ten hours in *E. coli*. Furthermore, the GRAVY value was recorded at -0.134, indicating that the vaccine construct is hydrophilic, as shown in Fig. 7 below.

(A)

Amino acid composition		
Amino acids	**Percentage**	**Number**
Ala (A)	12.2%	43
Arg (R)	5.9%	21
Asn (N)	2.5%	9
Asp (D)	2.8%	10
Cys (C)	2.0%	7
Gln (Q)	3.4%	12
Glu (E)	4.0%	14
Gly (G)	7.6%	27
His (H)	2.0%	7
Ile (I)	7.4%	26
Leu (L)	7.4%	26
Lys (K)	8.5%	30
Met (M)	1.7%	6
Phe (F)	5.4%	19
Pro (P)	2.0%	7
Ser (S)	5.7%	20
Thr (T)	3.7%	13
Trp (W)	0.6%	2
Tyr (Y)	10.8%	38
Val (V)	4.5%	16

(B)

Atomic Composition	
Carbon C	1862
Hydrogen H	2835
Nitrogen N	483
Oxygen O	494
Sulfur S	13

(C)

Physico-chemical properties	
Total number of atoms	5687
Number of amino acids	353
Molecular weight	40307.71
Theoretical pI	9.63
Instability index	23.71
Grand average of hydropathicity (GRAVY)	-0.134
Solubility in *Escherichia coli*	0.830

Fig. 7. (**A**) The concentration of amino acids, (**B**) The atomic composition, and (**C**) Physico-chemical characteristics of the vaccine construct by using the ExPASy ProtParam server.

Secondary structure of vaccine

The secondary structure of the vaccine construct was predicted using PSIPRED and GOR-IV servers. PSIPRED shown in Fig. 8 (A) highlights secondary structure elements, with alpha helices[69], beta strands (yellow), and coils (gray), along with functional annotations such as disordered regions, protein binding sites, and membrane interactions. The GOR-IV pie chart Fig. 8 (B) quantifies structural composition, showing alpha helices (45.61%), beta strands (17.85%), and coils (36.54%), indicating a predominantly helical structure. The interaction graph Fig. 8 (C) illustrates fluctuations in helices, sheets, and coils along the sequence, confirming a well-structured and potentially stable protein. These insights are crucial for evaluating the vaccine candidate's structural integrity, stability, and immunogenic potential.

Tertiary structure of vaccine

TrRosetta predicted five different models, and as shown in Fig. 9 (A), the model with the highest C-score of 7.167 exhibited a TM-score of 0.52 ± 0.25 was selected. The structure of the improved 3D model is illustrated in Fig. 9 (B). The Ramachandran plot statistics for the vaccine construct were analyzed using the PROCHECK tool. The results indicated that approximately 97.4% of the residues were in the most favored regions, while 2.3% were in the additionally allowed zones. Only 0.3% of the residues were located in the disallowed regions, as shown in Fig. 9 (C). The total quality factor value of the improved 3D structures, estimated using ERRAT was 97.078 (Fig. 9D).

Prediction of discontinuous B-Cell epitopes using ellipro

Ellipro analysis predicted eight discontinuous B-cell epitopes in the vaccine construct, as illustrated in Fig. 10, with scores between 0.501 and 0.967, as shown in Table 5 below, which reflects their antigenic potential. The highest-scoring epitope (0.967 scoring 22 residues) is immunodominant and most likely to be found in the proximal surface, and immunogenic longer epitopes, such as the 40-residue epitope (score: 0.732), may contribute to strong immune recognition. Shorter low-scoring epitopes might be less immunogenic but still involved in antibody recognition.

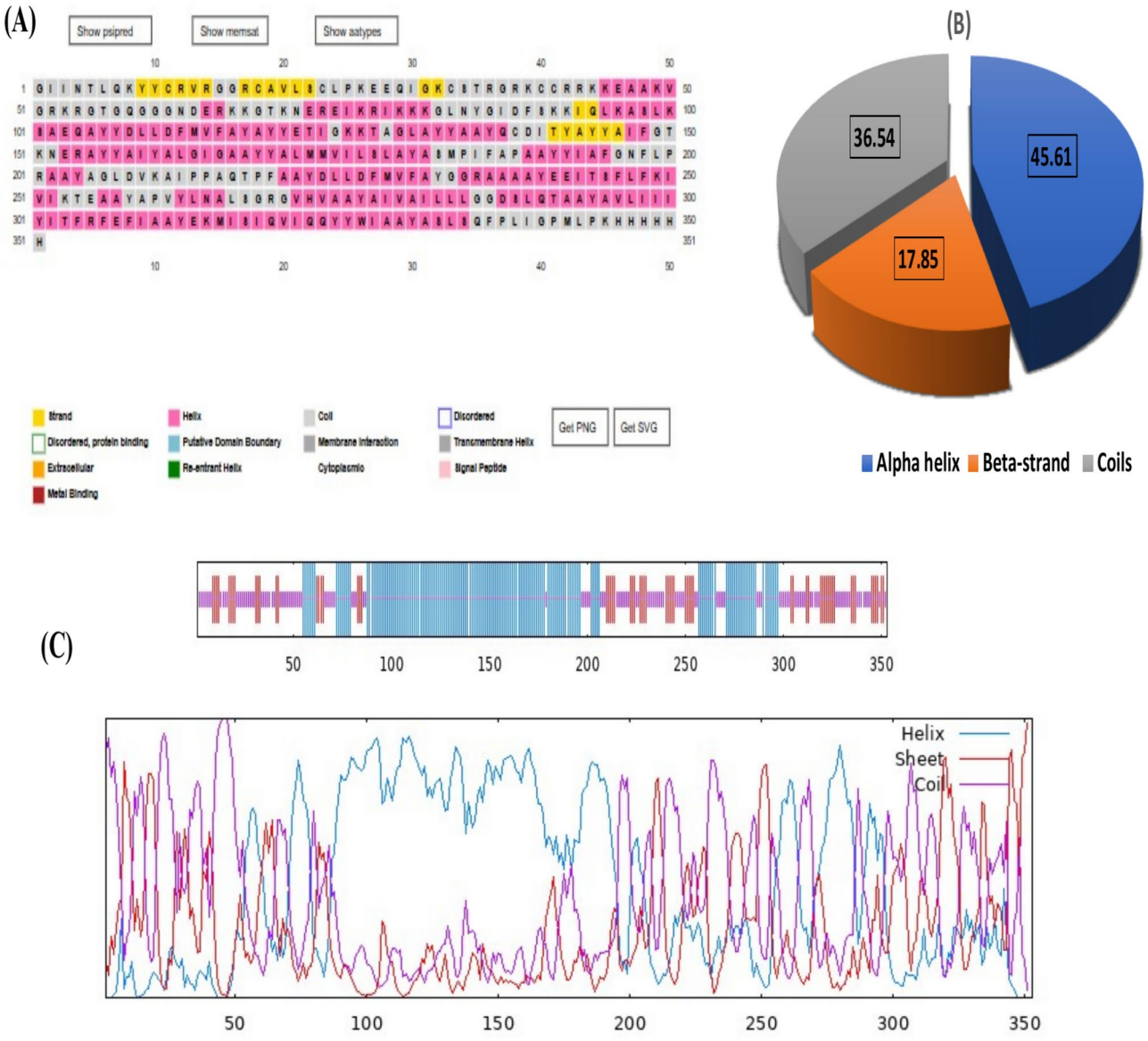

Fig. 8. Predicted Secondary Structure of the Vaccine Construct: **(A)** PSIPRED visualization with helices, coils (grey), and beta strands (yellow). **(B)** GOR-IV pie chart showing structural distribution. **(C)** Illustration of amino acid interactions in helices, sheets, and coils.

Disulfide engineering

Disulfide engineering was performed by using Ser133–Ser145 pairs (energy: 0.68 kcal/mol) and Gly193–Ile208 (energy: 1.29 kcal/mol) as optimal residues in the vaccine construct, as shown in Fig. 11. The relatively lower energy of Ser133–Ser145 indicates more stability, which provides additional support for structural stiffness. On the other hand, Gly193–Ile208, with slightly higher energy, introduces moderate strain but remains within an acceptable range. These engineered bonds enhance the vaccine's stability, reducing degradation and potentially improving immunogenicity.

Analysis of molecular docking for the constructed vaccine

The refined tertiary structure of the vaccine construct was docked with TLR-3, TLR-4, TLR-7, and TLR-8 using ClusPro, as shown in Fig. 12. Using Cluspro, the vaccine construct was individually docked with each receptor. The tool provides us with 30 docked models from which the model having the lowest energy was selected. he docking results demonstrated specific interaction energies for all four receptor-vaccine complexes, including TLR-3, TLR-4, TLR-7, and TLR-8. The energy values for all four complexes are presented in Table 6.

In-depth analysis of Interactions in Docked Complexes

To evaluate the interactions of all the docked complexes, LigPlot was utilized. The analysis revealed that TLR-3 and TLR-4 demonstrated weak binding with the vaccine formulation, and TLR-7 and TLR-8 showed robust

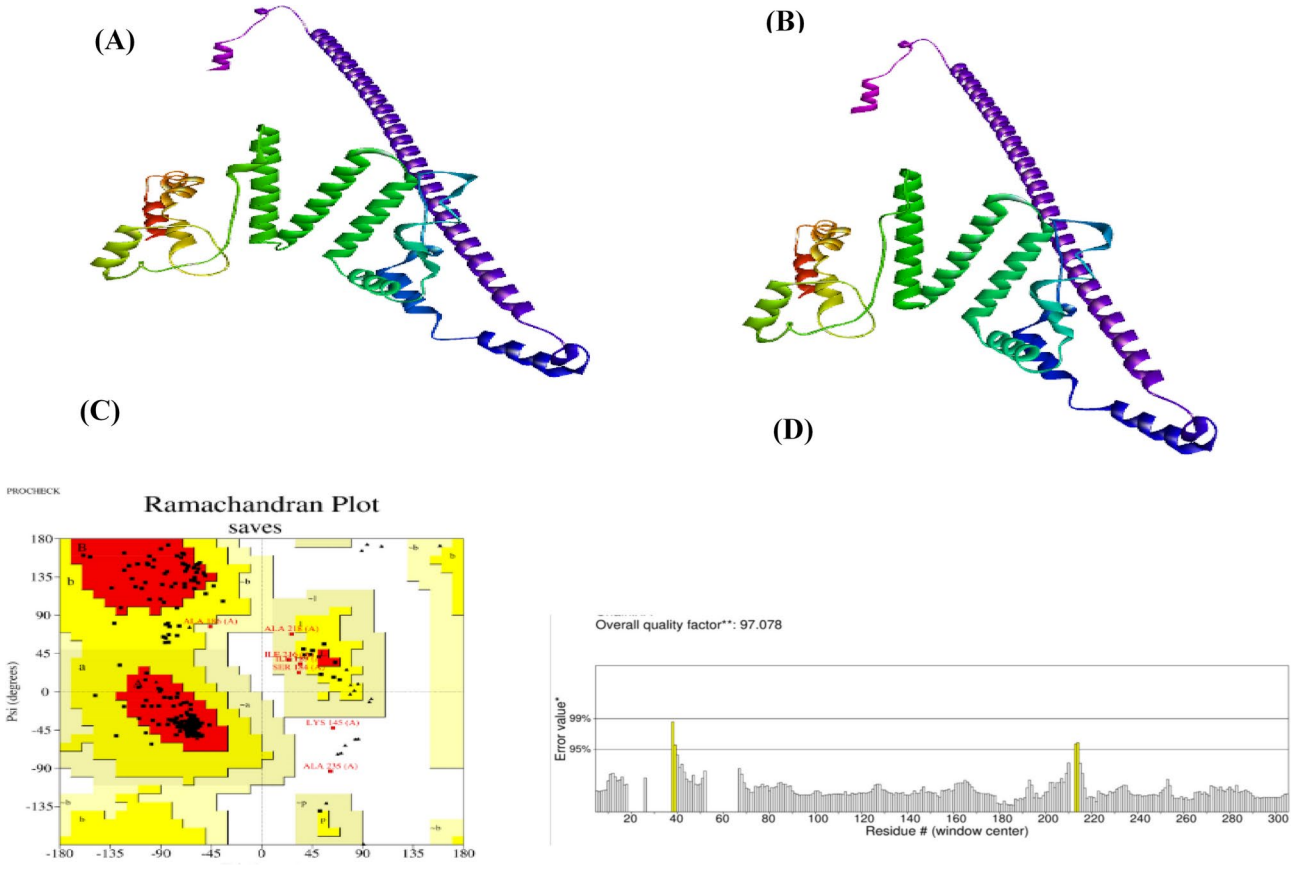

Fig. 9. **(A)** 3D visualization of the vaccine construct predicted by I-TASSER and visualized by discovery studio visualizer v24.1.0 (https://discover.3ds.com/discovery-studio-visualizer-download) **(B)** The refined model was created by Galaxy Refine and visualized by discovery studio visualizer v24.1.0 (https://discover.3ds.com/discovery-studio-visualizer-download) **(D)** Structure assessment was conducted using the Procheck program and **(D)** Quality analysis of the selected structure evaluated by the ERRAT available at UCLA-DOE LAB — SAVES v6.1 (https://saves.mbi.ucla.edu/).

binding. In interaction analysis, TLR-8(B) indicated 13 hydrogen bonds, while TLR-7 indicated12, as illustrated in Table 7. The analysis of amino acid interactions between Chain B of TLR8 and Chain V (vaccine) is presented in Fig. 13. The figure illustrates the interaction sites of the vaccine with the receptor's B chains, highlighting the bonds formed at these interaction points.

Molecular dynamic simulations

The MD simulations were performed using the DESMOND tool (Schrödinger). The system was solvated in a TIP3P water box with a 12 Å buffer in each dimension. NaCl ions were added to neutralize the system and maintain physiological conditions. The system underwent 20,000 steps of energy minimization using the steepest descent algorithm. The simulations were conducted under the NPT ensemble at a constant temperature of 298 K and pressure of 1 bar. The Langevin thermostat was used for temperature control, and the Martyna-Tobias-Klein barostat was used for pressure control. The Particle Mesh Ewald (PME) method was employed for long-range electrostatic interactions, with a cutoff of 9 Å for short-range interactions. The SHAKE algorithm was used to constrain fast-moving bonds. The simulation was run for 100 ns, and trajectories were saved every 10 ps. As shown in Fig. 14, the RMSD graph showed the structural stability of the designed vaccine and TLR8 complex over 500 ns of MD simulations. Initially, the RMSD was approximately approximately 0 Å, and it rises to 3–4 Å after 50 ns, indicating initial structural changes and equilibration. A notable peak between 100–120 ns suggests some form of conditional change or flexibility due to the RMSD reaching 7–8 Å. After 150 ns, the RMSD stabilizes around 3–5 Å, indicating that the system has reached equilibrium. The peak around 100–120 ns is flexible due to the stabilized complex changing from loop movements or minor domain rearrangement.

The stability after 150 ns further suggests that the designed vaccine interacts strongly with TLR8 while not causing too much destabilization within the system. At the end of the simulation from 400 to 500 ns, the RMSD remains constant around 4–5 Å, confirming the structural stability of the vaccine-TLR8 complex. An RMSD value between 3 and 5 Å indicates structural stability, suggesting that the complex will likely remain unchanged. This increases the likelihood of the vaccine being a good candidate for additional immunoinformatics study and subsequent experimental confirmation.

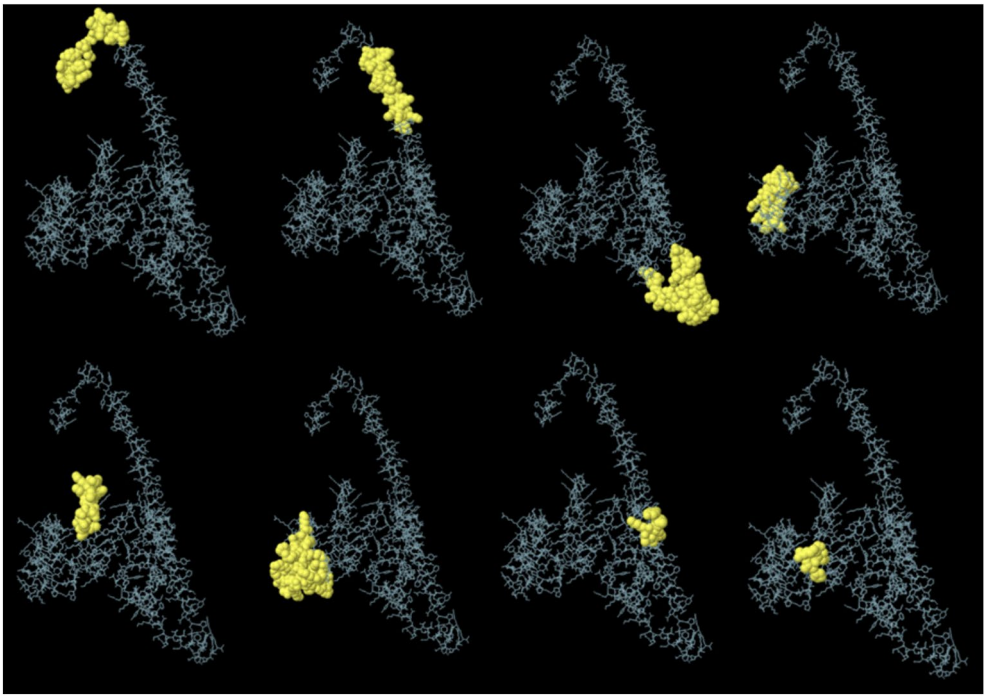

Fig. 10. Predicted Discontinuous B-Cell Epitopes. The images were captured from Ellipro server (http://tools.iedb.org/ellipro/) and Figure was created on MS word.

No	Residues	Length	Score
1	A:Y351, A:L352, A:P353, A:A354, A:S355, A:L356, A:S357, A:Q358, A:F359, A:P360, A:L361, A:I362, A:G363, A:P364, A:M365, A:L366, A:H367, A:H368, A:H369, A:H370, A:H371, A:H372	22	0.967
2	A:S316, A:G318, A:K319, A:E320, A:L321, A:K322, A:T323, A:S324, A:A325, A:I326, A:Y327, A:A328, A:L329, A:G330, A:A331, A:Y332, A:Y333, A:L334, A:F335, A:L336, A:S337, A:S338, A:C339, A:S340, A:S341, A:V342, A:N343, A:K344, A:E345, A:I346, A:S347, A:E348, A:A349, A:Y350	34	0.795
3	A:Y225, A:E229, A:N230, A:I231, A:S232, A:T233, A:G234, A:A235, A:S236, A:N237, A:D238, A:I239, A:Q240, A:A241, A:Y242, A:Y243, A:F244, A:M245, A:L246, A:R247, A:G248, A:V249, A:G250, A:K251, A:G252, A:G253, A:G254, A:G255, A:G256, A:P257, A:Q258, A:A259, A:Y260, A:Y261, A:E262, A:T263, A:I264, A:Q265, A:E267, A:I268	40	0.732
4	A:G1, A:I2, A:I3, A:N4, A:T5, A:L6, A:Q7, A:K8, A:Y9, A:Y10, A:C11, A:R12, A:V13, A:G15, A:G16, A:R17, A:C18, A:A19, A:V20, A:L21, A:S22, A:C23, A:L24, A:P25, A:K26, A:Q29	26	0.704
5	A:K85, A:D86, A:H87, A:S88, A:D89, A:L90, A:V91, A:Y92, A:K93, A:T94, A:K95, A:E97, A:K98	13	0.676
6	A:K32, A:C33, A:S34, A:T35, A:G37, A:R38, A:C41, A:K44, A:K45, A:G46, A:P47, A:G48, A:P49, A:G50, A:L51, A:G53, A:Q55, A:G57, A:D58, A:M59, A:F60, A:E61, A:R62, A:K63, A:Y64, A:Y65, A:S66, A:E67, A:Q68, A:T69, A:G70, A:K71, A:E72, A:I73, A:D74, A:D75, A:V76, A:K77, A:K78	39	0.657
7	A:F196, A:A197, A:K198, A:A199, A:A200, A:Y201, A:L202	7	0.583
8	A:P81, A:V82, A:I83, A:R84	4	0.501

Table 5. Residues of Predicted Discontinuous B Cell Epitopes.

The Root Mean Square Fluctuation (RMSF) graph, as shown in Fig. 15, indicates the flexibility of individual residues in the vaccine-TLR8 complex during molecular dynamics simulation. The average RMSF across the complex is maintained at approximately 1.5–2.5 Å, supporting overall structural stability. Many residues have low RMSF values, suggesting a stable structure over time (less than 2 Å). However, some notable exceptions exist, such as near residues 350, 750, 800, and 850. The highest fluctuation was observed around 8 Å near residue 850. These regions are most probably structured loops or less ordered regions in proteins. The N-domain and the central area (1–600) remain stable, suggesting that strong interactions between the vaccine and TLR8 are maintained, whereas the C-terminal region (750–900) is considerably flexible, which may affect antigen recognition.

The Radius of Gyration (Rg) graph provides the stability and compactness of the vaccine-TLR8 complex throughout the molecular dynamic simulation, as shown in Fig. 16. The values of Rg change between 35.0 Å and 37.5 Å, with a mean value close to 36.0 Å, which shows that the complex is likely to maintain a stable conformation. First, some small minor fluctuations reach 37.5 Å around 100 ns; Rg stabilizes after 200 ns, indicating that the structure is likely statically compact at this time. The slight increase in Rg after 400 ns indicates that some degrees of minor folds take place in the later stages of the simulation rather than significant unfolding. The overall results showed that vaccine-TLR8 complex vaccine-TLR8 complex retains its integrity throughout the simulation, with no significant structural collapse or excessive flexibility.

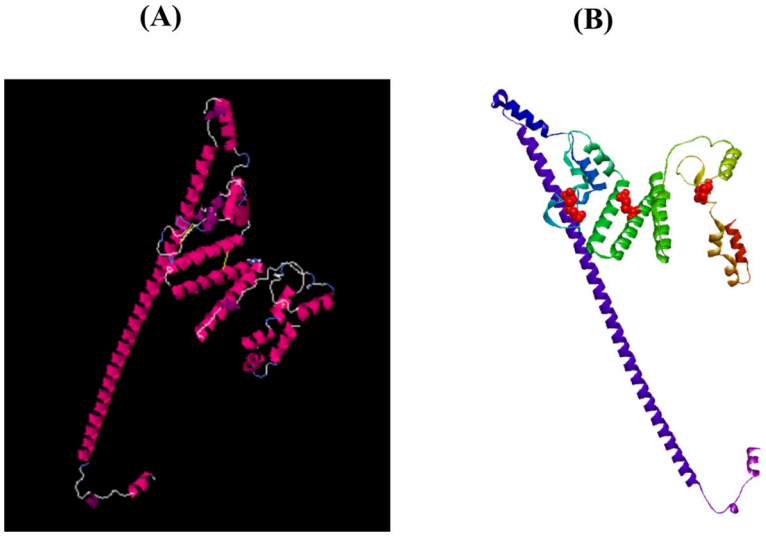

Fig. 11. **(A)**Yellow lines show the engineered disulfide bonds predicted by Disulfide by Design 2.0 (http://cptweb.cpt.wayne.edu/DbD2/). This image was directly captured from Disulfide by Design 2.0 server **(B)** Red-colored ball residues represent the two mutated pairs visualized by using discovery studio visualizer v24.1.0 (https://discover.3ds.com/discovery-studio-visualizer-download).

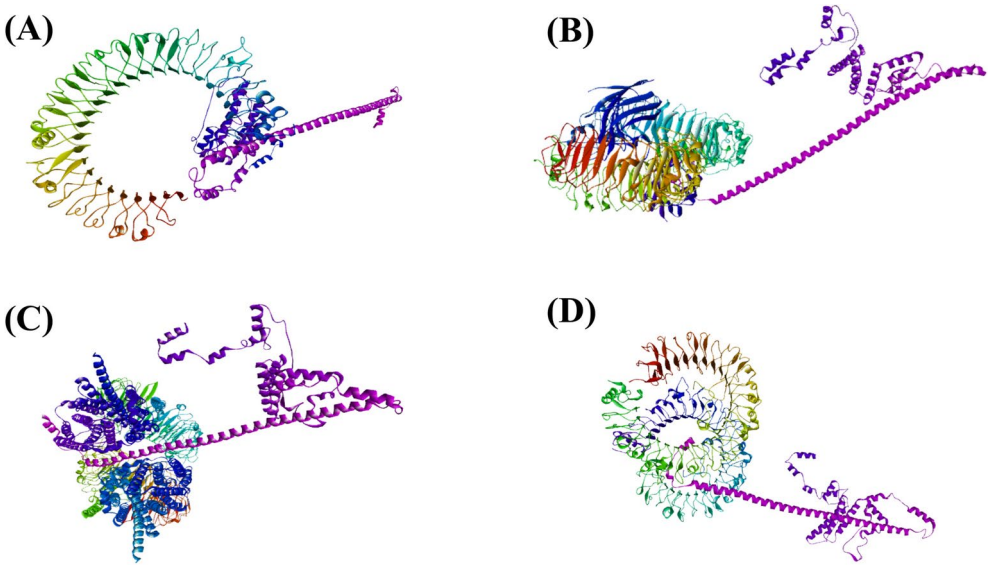

Fig. 12. Docked complexes of TLR-3, TLR-4, TLR-7, and TLR-8 with the designed vaccine visualized by using discovery studio visualizer v24.1.0 (https://discover.3ds.com/discovery-studio-visualizer-download). **(A)** The docked complex of TLR-3 with the vaccine design. **(B)** The docked complex of TLR-4 with the vaccine design. **(C)** The docked complex of TLR-7 with the vaccine design. **(D)** The docked complex of TLR-8 with the vaccine design.

Docked complex of receptors with vaccine	Energies (kcal/mol)
TLR 3	-1151.7 kcal/mol
TLR 4	-1479.9 kcal/mol
TLR 7	-2043.7 kcal/mol
TLR 8	-1434.6 kcal/mol

Table 6. Docked energies with vaccine construct.

Sr. No	Res Name	Residue No	Chain		Res. Name	Residue No	Chain	Distance Å
1	ARG	650	B	--	ILE	362	V	2.740
2	ARG	650	B	--	ILE	362	V	2.794
3	GLN	358	V	--	ASP	627	B	2.786
4	ARG	619	B	--	PRO	360	V	2.775
5	ARG	619	B	--	LEU	361	V	2.778
6	ARG	619	B	--	PRO	360	V	2.689
7	THR	600	B	--	ALA	349	V	2.667
8	HIS	576	B	--	ALA	349	V	2.896
9	HIS	367	V	--	ARG	569	B	2.797
10	ARG	569	B	--	HIS	370	V	2.654
11	ARG	569	B	--	HIS	370	V	2.746
12	ASN	546	B	--	GLU	345	V	2.948
13	TYR	350	V	--	ASP	543	B	2.804

Table 7. Hydrogen bonds between Vaccine and chain A of TLR8 receptor.

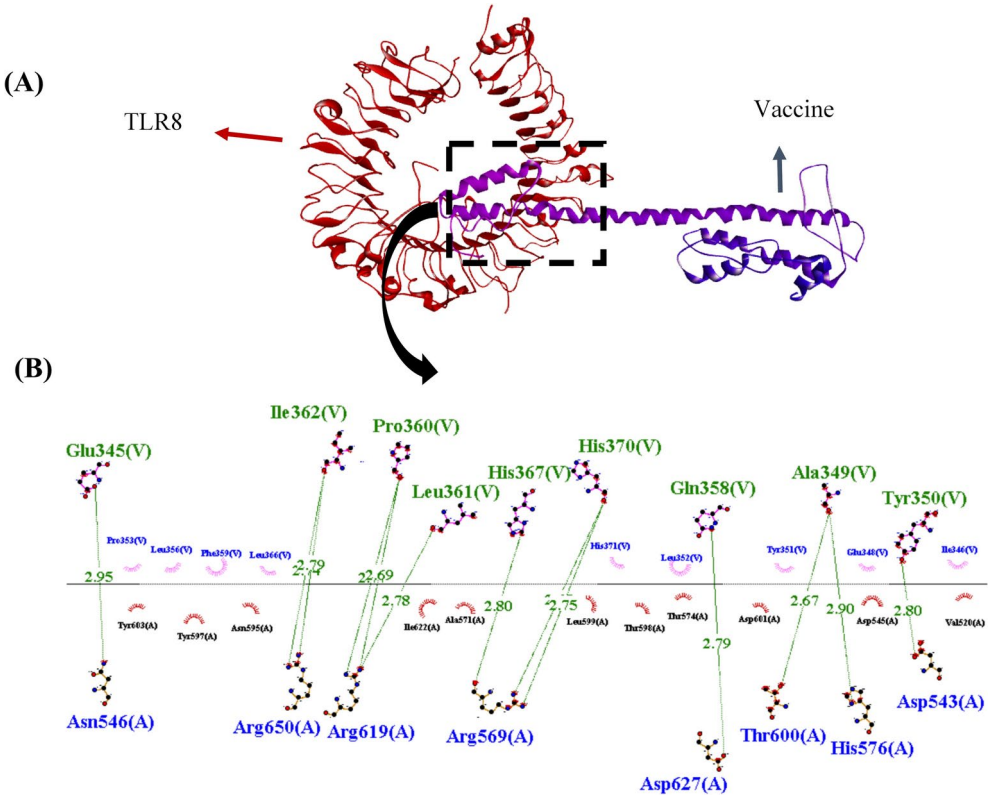

Fig. 13. **(A)** Docking complex of Chain B (TLR7) with chain V (Vaccine) visualized by discovery studio visualizer v24.1.0 (https://discover.3ds.com/discovery-studio-visualizer-download) **(B)** Interactions analysis by using Ligplot + v.2.2 (https://www.ebi.ac.uk/thornton-sr v/software/LigPlus/).

Principal component analysis

The principal component analysis (PCA) scatter plot visualizes the distribution of data points based on principal component analysis PCA, where PC1 and PC2 represent the first two principal components, as shown in Fig. 17. The clustering in the center is a high-density region, which indicates structural similarity in the vaccine-TLR8 complex. The dispersed points around the central cluster indicate the variations or conformational flexibility. The distinct clusters may indicate different binding modes or conformational states of the vaccine-TLR8 interactions. From this analysis, the structural diversity and stability of the vaccine-TLR8 complex are understood, which is essential for understanding its molecular behavior and possible immunogenic response.

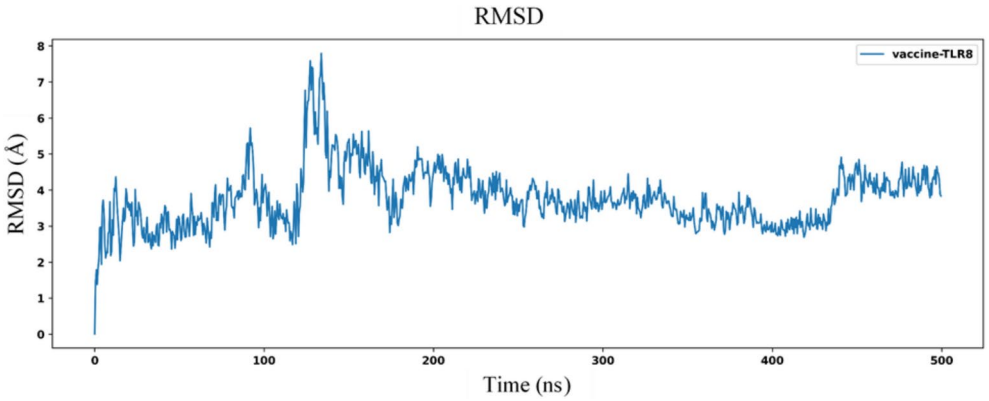

Fig. 14. RMSD graph of Vaccine-TLR8 complex over 500 ns of MD simulations.

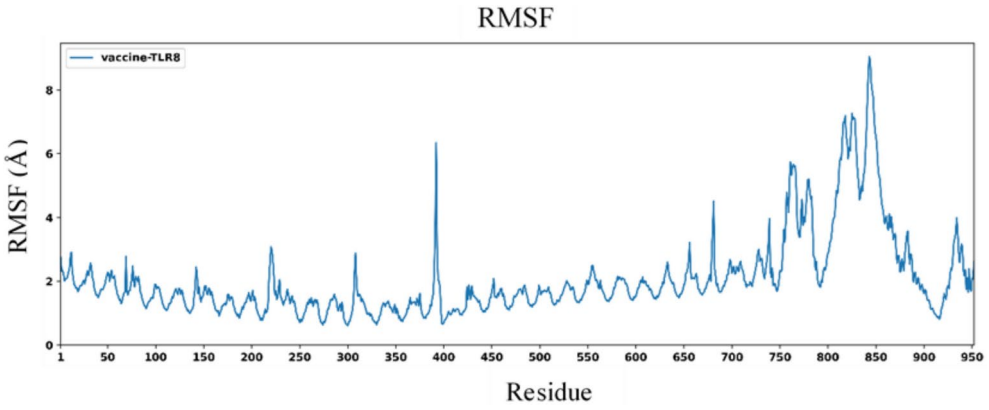

Fig. 15. RMSF graph of Vaccine-TLR8 complex over 500 ns of MD simulations.

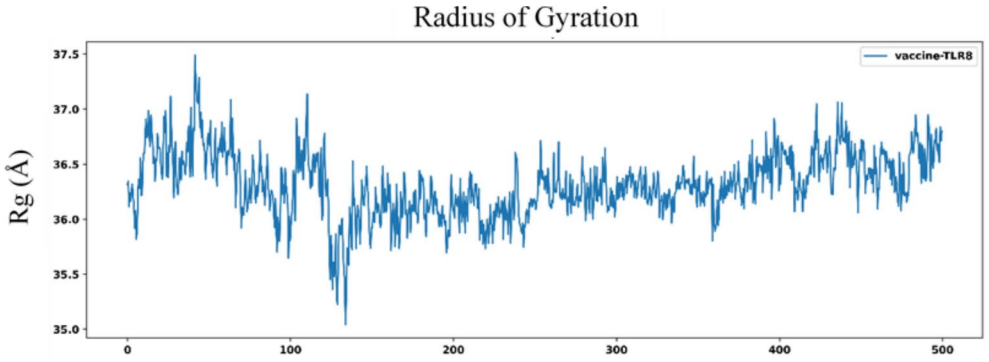

Fig. 16. Rg graph of Vaccine-TLR8 complex over 500 ns of MD simulations.

MM/PBSA

The MM/PBSA energy plot measures the binding free energy of the vaccine-TLR8 complex during the simulation period, providing the stability and interaction strength of the complex. The binding energy fluctuates from -1000 kJ/mol to -7000 kJ/mol with an average of around -5000 kJ/mol, showing a stable and strong interaction as shown in Fig. 18. Even though there are occasional energetic peaks, the system consistently returns to stable energy levels of -5000 kJ/mol, which confirms the reliability of the binding. The Lower binding energy values correlate with stronger binding affinity, suggesting that the vaccine remains tightly associated with TLR8 throughout the simulation. The presence of stable energy levels confirms the stability of the vaccine-TLR8 interactions throughout the simulations.

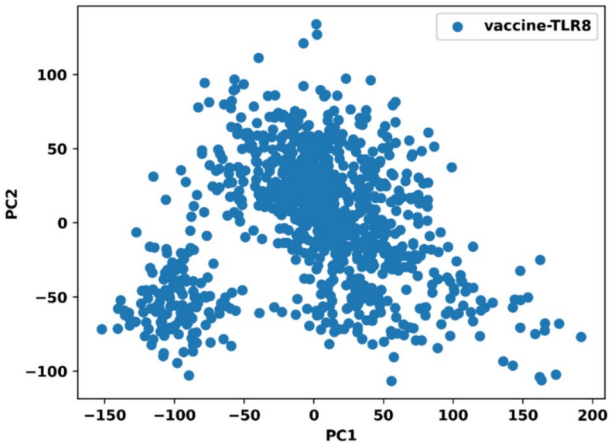

Fig. 17. PCA plot of Vaccine-TLR8 complex over 500 ns of MD simulations.

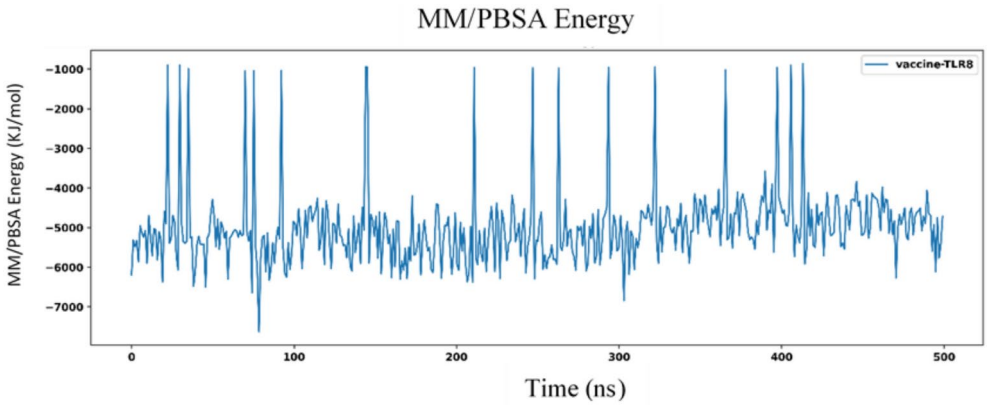

Fig. 18. MM/PBSA graph of Vaccine-TLR8 complex over 500 ns of MD simulations.

DCCM

As shown in Fig. 19 (A), the dynamical cross-correlation matrix (DCCM) plot of the vaccine-TLR8 complex reveals correlated and anti-correlated motions of residues during molecular dynamics simulations. Dark blue regions (1.0) represent extreme correlation, suggesting that some motion ensures structural stability, while light yellow regions (-1.0) suggest anti-correlated motions, which show highly flexible domains. Distinct correlation blocks highlight structured domain interactions, contributing to the complex's stability. These Uncorrelated regions suggest independent movements and may correlate with functional flexibility. The results confirm that the vaccine maintains a stable interaction with TLR8 while allowing necessary conformational dynamics for its biological function and activation of the immune system.

Free energy landscape

The 3D FEL plot shows the energy variations of different conformational dynamics of the vaccine-TLR8 complex. The color scale ranges from blue (low Gibbs free energy) to red (high energy), indicating conformational stability, as shown in Fig. 19 (B). A high-density red cluster around (PC1 ≈ 0, PC2 ≈ 0) suggests an average energy of ~ 1.5 kJ/mol. The scattered blue regions at higher energy (~ 8 kJ/mol) show the average value of the transient conformational shifts. This contour plot displays the distribution of Gibbs free energy over the two central components (PC1 and PC2), demonstrating the complex's principal movements, as shown in Fig. 19 (C). The most stable conformations, or the regions where the complex spends most of its simulation time, are red ~ 1.1 kJ/mol areas. The blue areas (~ 7.9 kJ/mol) correspond to higher energy states, representing transient fluctuations. From this dataset, the average Gibbs free energy was calculated at 3.0 kJ/mol, which provides additional evidence that the complex is still thermodynamically stable but shows signs of conformational flexibility.

The scatter plot shows a distinct distribution of points defined by their conformation with free energy levels, which presents stability patterns, as shown in Fig. 19 (D). The red cluster of points with high density located at (PC1 ≈ 0, PC2 ≈ 0) has an average energy of ~ 1.5 kJ/mol, which shows that the system is mainly in a stable basin of low energy. The blue points scattered around the plot (~ 8.0 kJ/mol) show transient high-energy oscillations, indicating that the system periodically goes to high-energy unfavorable states. The average Gibbs free energy calculated from this dataset is 3.2 kJ/mol, which means the vaccine-TLR8 complex's stability with minimal

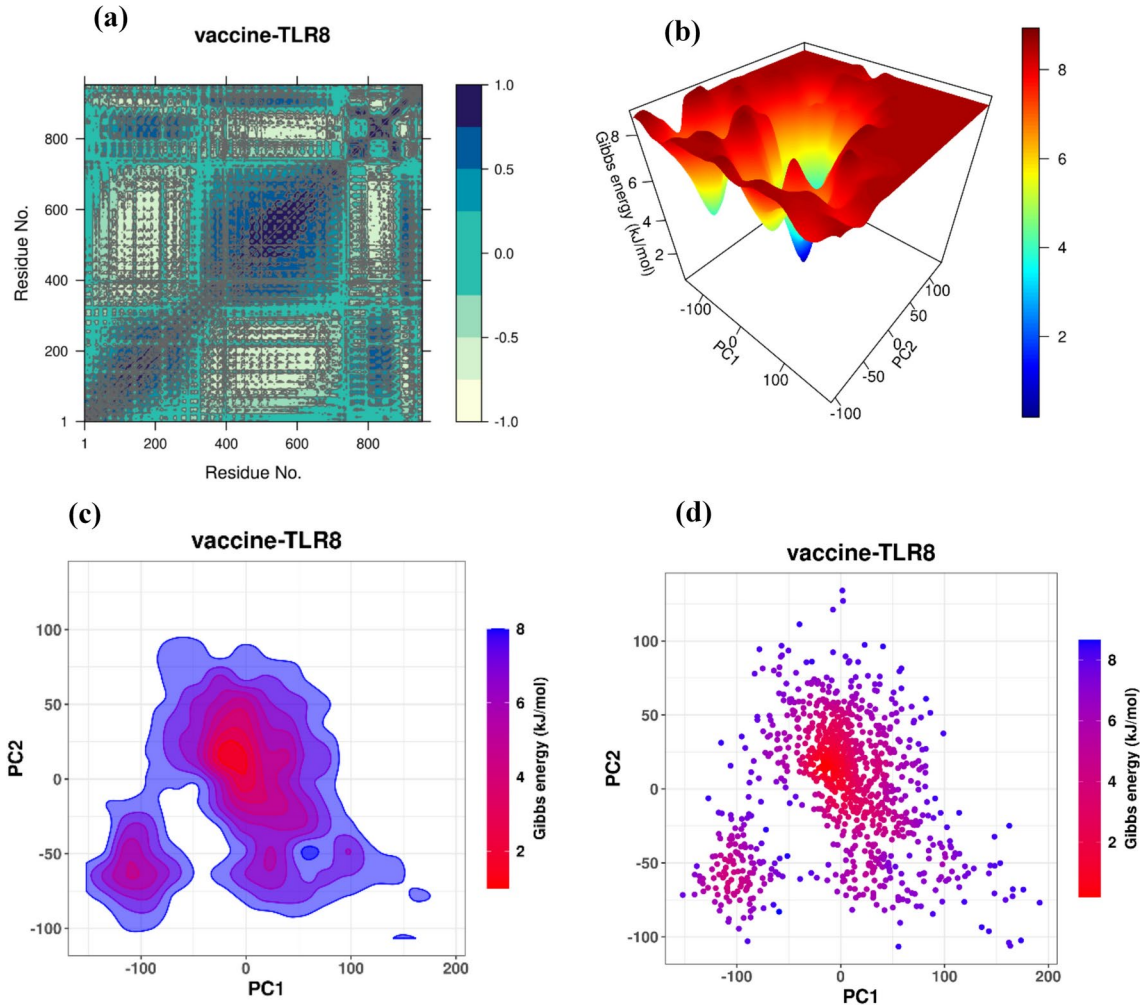

Fig. 19. **(A)** Dynamic Cross-Correlation Matrix (DCCM) **(B)**Three-Dimensional Free Energy Landscape of the vaccine-TLR8 complex **(C)** Two-Dimensional Free Energy Landscape (2D FEL Contour Plot) **(D)** Gibbs Free Energy Scatter Plot . All the plots were created by using bio3Dv2.4–2 package in R (http://thegrantlab.org/bio3d/).

energy variations. These findings confirm that the vaccine construct is structurally stable and energetically favorable, making it a strong candidate for effective immune activation through TLR8 binding.

Codon optimization

Codon optimization was done to increase the expression of the designed vaccine in the *E.coli* strain K12. The GC content of the optimized sequence was reduced from 61.85% to 41.72%, which falls within the optimal range of 30–70% for *E. coli* expression. To ensure that the optimized sequence does not form stable secondary structures that could hinder transcription or translation, we analyzed potential mRNA folding issues using the RNAfold server. The results that the free energy of the thermodynamic ensemble was -438.35 kcal/mol, with an ensemble diversity of 334.69, and the frequency of the MFE structure in the ensemble was 0.00%, supports the high translational efficiency of the optimized sequence, as given in Fig. 20.

In silico *cloning of vaccine construct*

The 1059 base pairs DNA sequence was successfully cloned into pET-29(+) vector, which has a total size of 5371 base pairs, using SnapGene. The vector was cut with the Akani restriction enzyme, and the vaccine construct was inserted at position 5001. After cloning the total length of the recombinant vector increased to 6430 bp as shown in Fig. 21.

Immune simulation of vaccine construct

In the host mammalian body, viral antigens presented in the designed vaccine triggered immune. Several parabiotic graphs display the number of cells, increased IgM concentrations, and various simulated effects on B cells, as well as MHC-I and MHC-II per milliliter in the body. An increase in B cell numbers was observed, directly correlating with the rise in both total and specific antibody production especially Ig G1, Ig G2, Ig M,

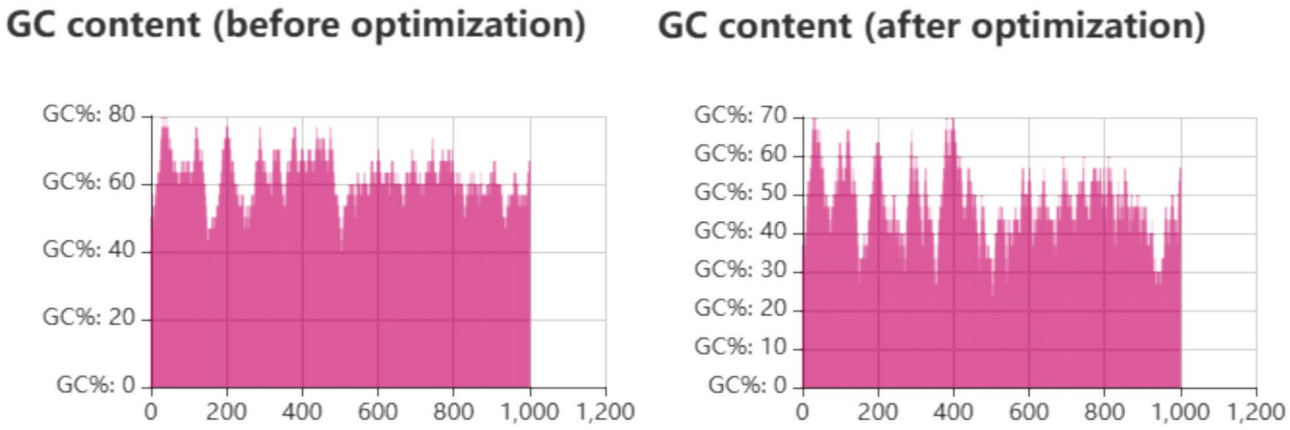

Fig. 20. Codon optimization by Codon Optimization Tool (ExpOptimizer)().

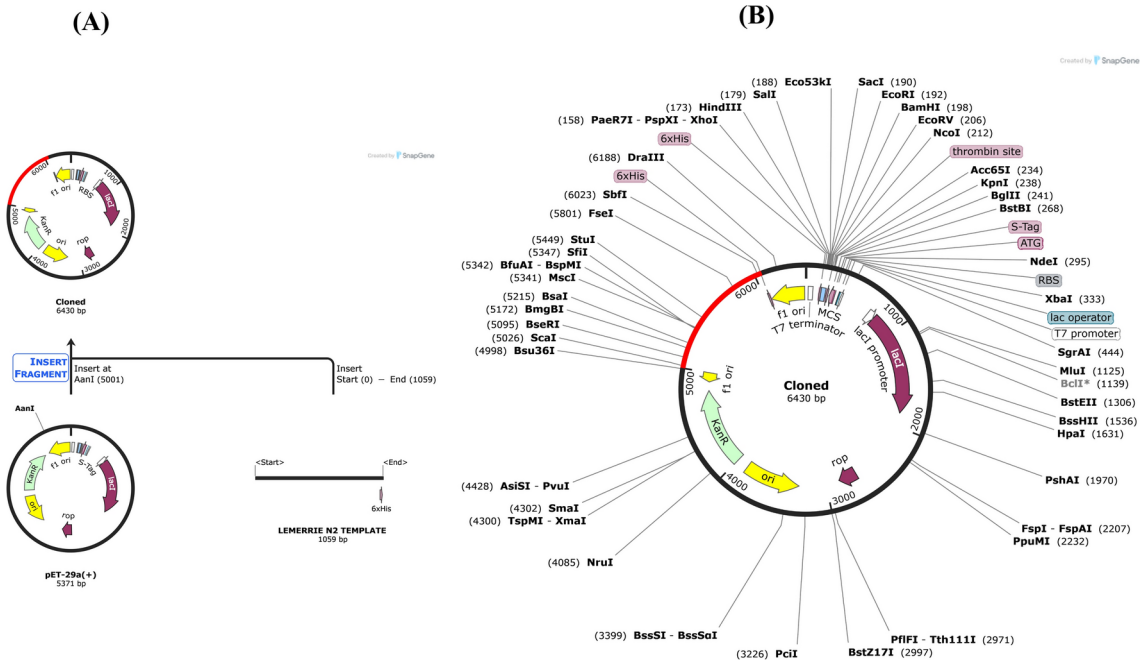

Fig. 21. Cloning history and cloned plasmid representing all restriction sites with insertion of vaccine construct in pET-29a(+) performed by using SnapGene 8.0.0 software (https://www.snapgene.com/).

and Ig G/IgM. As shown in Fig. 22, the level of cytokines and interleukins as well as the leukocyte growth factor IL-20 signaling an immune response. Post-vaccination analysis also showed a significant increase in IFN-γ levels, confirming a strong immunological reaction against *Fusobacterium necrophorum*. The simulation results indicate that antigen production begins around day 3, while antibody production starts around day 7, peaks at approximately 3,000 units, and continues to rise, reaching a maximum of 5,000 units by day 14.Interleukins, cytokines, and growth factors such as IL-20 and IFN-γ play pivotal roles in modulating and enhancing the immune response. IL-20 contributes to tissue inflammation and repair, acting as a danger signal to activate and recruit immune cells. IFN-γ, a key cytokine of the Th1 immune response, enhances macrophage activation and antigen presentation, promoting the clearance of intracellular pathogens such as *Fusobacterium necrophorum*. These immune mediators work synergistically to stimulate phagocytosis, improve adaptive immune responses, and eradicate the present pathogen.

Discussion

Fusobacterium necrophorum is an anaerobic, gram-negative pathogen that causes Lemierre's syndrome in humans and bovine foot rot in livestock[70]. The emerging antimicrobial resistance (AMR) in *Fusobacterium necrophorum* is concerning due to the absence of effective vaccines, requiring a new need for alternate treatments[71]. Recently, computational vaccine design has become a cost-effective and rapid approach for designing multiepitope

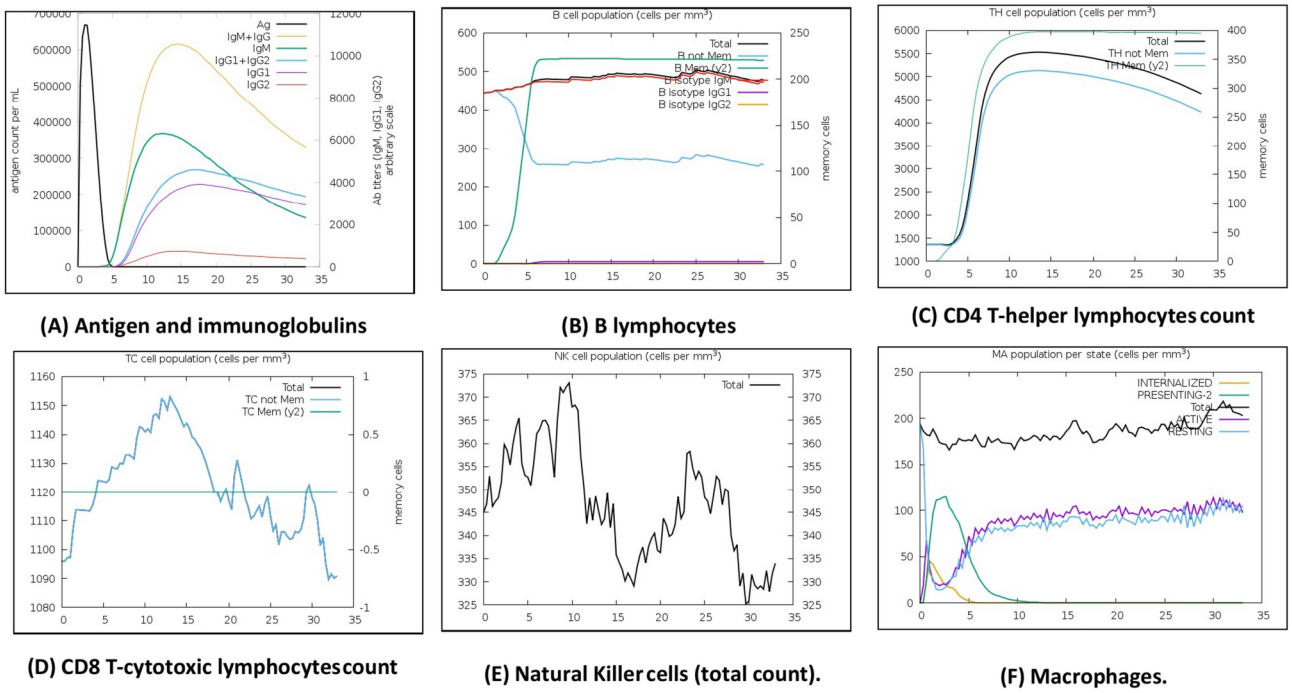

Fig. 22. Immune simulation results predicted by using the C-IMMSIM server.

vaccines[72]. Similarly, in this study, we utilized Immunoinformatics, molecular docking, and molecular dynamics simulations to design a multiepitope vaccine utilizing transmembrane proteins of *F. necrophorum*, with the results showing strong antigenicity, receptor binding, structural stability, and immunogenic prediction.

In designing a multiepitope vaccine against *Fusobacterium necrophorum*, we identified 4 B-cell epitopes, 8 MHC class I epitopes, and 8 MHC class II epitopes to elicit comprehensive immune responses. The vaccine construct has a molecular weight of approximately 61.48 kDa and an isoelectric point (pI) of 9.92, indicating a basic nature. A GRAVY value of 0.001 suggests balanced hydrophilicity and hydrophobicity, while an aliphatic index of 82.45 reflects high thermostability. The antigenicity score of our vaccine construct was 0.7293 (VaxiJen analysis), which classifies it as highly immunogenic. Also, the population coverage estimates showed values of 99.39%, ensuring the applicability across different ethnicities. These results correspond to the study of the Monkeypox vaccine wherein VaxiJen thresholds of > 0.4 were used for epitope selection. However, our vaccine construct showed a higher antigenicity score than the average Monkey pox score of 0.45[73].

Additionally, a previous study on the Klebsiella pneumoniae vaccine reported population coverage of 95%, which is lower than the current findings, suggesting the selected epitopes offer better global applicability[74]. Molecular docking analysis showed strong interactions between the vaccine construct and immune receptors, particularly TLR7 and TLR8, which play crucial roles in innate immune activation. Toll-like receptors (TLRs) are essential in recognizing pathogen-associated molecular patterns (PAMPs) and initiating innate and adaptive immune responses[75]. Among the various TLRs, TLR7 and TLR8 are particularly important in detecting bacterial and viral RNA, making them essential for an effective immune response against *F. necrophorum* infections. The TLR7-vaccine complex had 12 hydrogen bonds, whereas TLR8 showed the most potent interaction of 13 hydrogen bonds and -1434.6 kcal/mol binding energy. In comparison, these results suggest a stable and highly immunogenic interaction, aligning with previous studies on vaccine docking. For instance, a study on a multiepitope vaccine against Epstein-Barr virus (EBV) found TLR interactions of ~ 10–12 hydrogen bonds[76], slightly lower than our 13 hydrogen bonds with TLR8, suggesting that our vaccine construct may provide a more robust immune activation.

Molecular dynamics (MD) simulations were conducted for 500 ns to evaluate the stability and flexibility of the vaccine-TLR8 complex. The root mean square deviation (RMSD) stabilized around 4–5 Å, indicating minimal structural fluctuations after 150 ns, while the root mean square fluctuation (RMSF) analysis showed average flexibility (1.5–2.5 Å), except for minor fluctuations (8–9 Å at residue 850). Additionally, the radius of gyration (Rg) remained stable at ~ 36 Å, confirming no significant unfolding throughout the simulation. Comparing our findings with previous study by Swetha et al., 2022, a Monkeypox virus vaccine study reported an RMSD of 5–6 Å over 300 ns[73], which was slightly higher than our 4–5 Å over 500 ns, indicating that our vaccine construct may exhibit greater stability. Similarly, a Helicobacter pylori vaccine demonstrated RMSF values of 2–4 Å, slightly higher than our study (1.5–2.5 Å), suggesting that our vaccine structure may be more rigid and stable. Furthermore, MM/PBSA free binding energy calculations in a Neisseria gonorrhoeae vaccine study yielded an average of -4000 kJ/mol[77]. In contrast, our vaccine showed -5000 kJ/mol, confirming that our construct has stronger and more stable binding. This suggests that our construct has stronger, more stable binding than the others.

Immune simulation results suggested robust activation of both humoral and cellular immunity, with a peak IgM and IgG response reaching 5000 units by day 14. Additionally, cytokine analysis revealed high levels of IFN-γ, which plays a crucial role in pathogen clearance and immune activation. Moreover, analysis of cytokines showed elevated levels of IFN-γ, which is fundamental to immune mobilization and pathogen elimination. Our study findings are in line with other investigations, including a vaccine trial for Herpes simplex virus type-1 (HSV-1), where the peak levels of IgM/IgG attained reporting values of 4500[78], which is lower than the 5000, providing evidence for more and prolonged immune response Furthermore, the vaccine shows high expression in the pET-29(+) vector system, which is known for its strong T7 promoter-driven expression in *Escherichia coli* as Insilico expression of multiepitope vaccine was also performed in the previous study by Biswas et al*.,* 2024 [79].

Although the computational results are encouraging, experimental validation is needed to assess the immunogenicity and safety of the designed vaccine. In vitro analysis of antibody and cytokine response, as well as in vivo examination of protective efficacy in animal models, will help understand the entire scope of the vaccine's protective capabilities. In addition, the modification of immunogenicity adjuvants, primarily via TLR stimulation through CpG motifs, could also be investigated. Further research should also look into vaccine formulation approaches with improved bioactivity, like nanocarrier-based delivery systems, for enhanced stability and controlled vaccine release.

Conclusion

This study describes the capability of computational biology in developing a multiepitope vaccine against *F. necrophorum* , a pathogen causing severe infections in humans and livestock. By targeting transmembrane proteins, Insilco tools identified non-toxic, antigenic, and non-allergenic epitopes connected to form a strong vaccine construct. Codon optimization and in silico cloning enhanced vaccine stability and expression in host cells. Immune simulations revealed strong activation of humoral and cellular immunity, including increased antibody production and cytokine release. Docking studies confirmed effective interactions with immune receptors like TLR-7 and TLR-8 that was further validated by MD simulations, highlighting the vaccine's potential to stimulate targeted immune responses. This computational approach offers a promising foundation for developing a vaccine against *F. necrophorum infections. However* Further in vitro and in vivo studies are required to assess immune responses, protective efficacy, and potential challenges in vaccine formulation and administration**.**

Limitations and future prospective

The predictions regarding antigenicity and immunogenicity require experimental validation. Future in-vitro and in-vivo validations are necessary to ensure its effectiveness. This research provides a valuable foundation for combating *F. necrophorum* infections through innovative vaccine development.

Data availability

All the data generated in this research work has been included in the manuscript. The FASTA sequences of target proteins of F. necrophorum was retrieved from UniProt database https://www.uniprot.org/. For the identificatio n of the antigenic characteristics of the viral protein, we utilized the web server Vaxijen 2.0 (https://www.ddg-p harmfac.net/vaxijen/VaxiJen/VaxiJen.html). The server allertop (https://www.ddg-pharmfac.net/allertop_test/) was used for the prediction of protein allergenicity. The IEDB server (http://tools.iedb.org/bcell/) was used to predict B-cell epitopes based on surface accessibility of antigen–antibody structures (Naveed et al., 2022). T-cell epitopes were analyzed using IEDB tools for MHC-I (http://tools.iedb.org/mhci/) and MHC-II (http://tools.ied b.org/mhcii/). The IEDB server (https://www.iedb.org/) was used to evaluate the population coverage of MHC Class I and Class II molecules in the population.

Received: 1 February 2025; Accepted: 25 April 2025
Published online: 04 May 2025

References

1. Fujiwara, N. et al. Involvement of fusobacterium species in oral cancer progression: a literature review including other types of cancer. *Intl. J. Mol. Sci.* **21**(17), 6207 (2020).
2. Wright, K. *Genomics and virulence factors of Fusobacterium necrophorum* (University of Westminster, 2016).
3. Hansberry, D. R. et al. Lemierre's syndrome: Acute oropharyngeal infection leading to septic thrombophlebitis of the internal jugular vein with pulmonary septic emboli. *Interdisciplinary Neurosurgery.* **19**, 100573 (2020).
4. Karacam, K., Demir, T. & Baris, O. Identification of dominant Bacteria isolated from periodontal abscesses. *J. Adv. Oral Res.* **13**(1), 91–96 (2022).
5. Alston, J. M. & Pardey, P. G. Agriculture in the global economy. *J. Economic Perspectives.* **28**(1), 121–146 (2014).
6. Rosander, A. et al. Prevalence of bacterial species associated with ovine footrot and contagious ovine digital dermatitis in Swedish slaughter lambs. *Acta Vet. Scand.* **64**(1), 6 (2022).
7. Carius, B. M., Koyfman, A. & Long, B. High risk and low prevalence diseases: Lemierre's syndrome. The *Am. J. Emergency Med.* **61**, 98–104 (2022).
8. Zhang, J. et al. Global, regional, and national burdens of HIV and other sexually transmitted infections in adolescents and young adults aged 10–24 years from 1990 to 2019: a trend analysis based on the Global Burden of Disease Study 2019. *Lancet Child Adolescent Health.* **6**(11), 763–776 (2022).
9. Jayasimhan, D., Wu, L. & Huggan, P. Fusobacterial liver abscess: a case report and review of the literature. *BMC Inf. Dis.* **17**, 1–9 (2017).
10. Nygren, D. *Fusobacterium necrophorum-from tonsillar carriage to Lemierre's syndrome* (Lund University, 2023).
11. Brook, I. Spectrum and treatment of anaerobic infections. *J. Inf. Chemotherapy.* **22**(1), 1–13 (2016).
12. Wong, N.S.T., *Characterization of the bacterial communities located on the skin surface of digital dermatitis and foot rot lesions of feedlot cattle*. (2023).

13. Bamouh, Z. et al. The prevalence, virulence, and serogroups of Dichelobacter nodosus and prevalence of Fusobacterium necrophorum in footrot lesions of sheep and cattle in Morocco. *Veterinary World.* **16**(4), 668 (2023).
14. Willis, Z. *The epidemiology of ovine footrot and virulence and phylogeny of Dichelobacter nodosus in a single flock and globally* (University of Warwick, 2019).
15. Wang, F.-F. et al. Fusobacterium necrophorum promotes apoptosis and inflammatory cytokine production through the activation of NF-κB and death receptor signaling pathways. *Front. Cell. Inf. Microbiol.* **12**, 827750 (2022).
16. Chenais, E. et al. Perceptions of pastoralist problems: a participatory study on animal management, disease spectrum and animal health priorities of small ruminant pastoralists in Georgia. *Preventive Veterinary Med.* **193**, 105412 (2021).
17. Gelbart, M. et al. Fusobacterium necrophorum as an emerging pathogen of acute mastoiditis. *Pediatric Inf. Dis. J.***38**(1), 12–15 (2019).
18. Mancuso, G. et al. Bacterial antibiotic resistance: the most critical pathogens. *Pathogens.* **10**(10), 1310 (2021).
19. Palma, M. & Qi, B. Advancing phage therapy: A Comprehensive review of the safety, efficacy, and future prospects for the targeted treatment of bacterial infections. *Inf. Dis. Rep.* **16**(6), 1127 (2024).
20. Lavalle, S. et al. Pediatric Lemierre's Syndrome: A Comprehensive Literature Review. *Pediatric Rep.* **16**(1), 201–213 (2024).
21. Zanolari, P. et al. Ovine footrot: A review of current knowledge. *Veterinary J.* **271**, 105647 (2021).
22. Pires, A. J. et al. When the solution becomes the problem: a review on antimicrobial resistance in dairy cattle. *Future Microbiol.* **19**(10), 903–929 (2024).
23. Chen, Y. et al. More than just a periodontal pathogen–the research progress on Fusobacterium nucleatum. *Front. Cell. Inf. Microbiol.* **12**, 815318 (2022).
24. Phelps, C., Chess-Williams, R. & Moro, C. The role of intracellular calcium and Rho kinase pathways in G protein-coupled receptor-mediated contractions of urinary bladder urothelium and lamina propria. *Am. J. Physiol-Cell Physiol.* **324**(3), C787–C797 (2023).
25. Pecoraro, C. et al. Recent developments in the inhibition of bacterial adhesion as promising anti-virulence strategy. *Intl. J. Mol. Sci.* **24**(5), 4872 (2023).
26. Van Zuylen, E. M. *Novel inhibitors for combating obligate anaerobic pathogens* (University of Otago, 2022).
27. Abdelhamid, A. G. & Yousef, A. E. Combating bacterial biofilms: current and emerging antibiofilm strategies for treating persistent infections. *Antibiotics.* **12**(6), 1005 (2023).
28. Krishnan, N. et al. Bacterial membrane vesicles for vaccine applications. *Adv. Drug Delivery Rev.* **185**, 114294 (2022).
29. Mortazavi, B., Molaei, A. & Fard, N. A. Multi-epitope vaccines, from design to expression; an in silico approach. *Human Immunol.* https://doi.org/10.1016/j.humimm.2024.110804 (2024).
30. Awadelkareem, E. A. & Hamdoun, S. Insilco vaccine design of spike and hemagglutinin esterase proteins of bovine coronavirus. *Transl. Med. Commun.* **9**(1), 28 (2024).
31. Khanum, S. et al. Mapping immunogenic epitopes of an adhesin-like protein from Methanobrevibacter ruminantium M1 and comparison of empirical data with in silico prediction methods. *Sci. Rep.* **12**(1), 10394 (2022).
32. Zhuang, S. et al. Bioinformatic prediction of immunodominant regions in spike protein for early diagnosis of the severe acute respiratory syndrome coronavirus 2 (SARS-CoV-2). *PeerJ* **9**, e11232 (2021).
33. Shams, M. et al. Engineering a multi-epitope vaccine candidate against Leishmania infantum using comprehensive Immunoinformatics methods. *Biologia* **77**(1), 277–289 (2022).
34. Elhag, M., et al., *Immunoinformatics Prediction of an Epitope Based Peptide Vaccine for Neisseria Gonorrhea Dihydrolipoamide Acetyltransferase Protein*. (2021).
35. Chutoam, P., Srisucharitpanit, K. & Intamaso, U. Investigating the Immunogenic Properties of a Mutagenized NS3/4A-Based HCV Genotype 3a DNA Vaccine. *Viral Immunol.* **38**(1), 1–11 (2025).
36. Ong, E. et al. Epitope promiscuity and population coverage of Mycobacterium tuberculosis protein antigens in current subunit vaccines under development. *Infect. Genet. Evol.* **80**, 104186 (2020).
37. Ullah, A. et al. Towards a novel multi-epitopes chimeric vaccine for simulating strong immune responses and protection against Morganella morganii. *Int. J. Environ. Res. Pub. Health.* **18**(20), 10961 (2021).
38. Motamedi, H., Shoja, S. & Abbasi, M. Immunoinformatic evaluation for the development of a potent multi-epitope vaccine against bacterial vaginosis caused by Gardnerella vaginalis. *PLOS ONE.* **20**(2), e0316699 (2025).
39. Samad, A. et al. Designing a multi-epitope vaccine against SARS-CoV-2: an immunoinformatics approach. *J. Biomole. Structure Dynamics.* **40**(1), 14–30 (2022).
40. Saadh, M. J. et al. Design of a novel multi-epitope vaccine candidate against Yersinia pestis using advanced immunoinformatics approaches: An in silico study. *Biochem. Biophys. Rep.* **40**, 101871 (2024).
41. Zhou, H. et al. Antimicrobial peptide A20L: in vitro and in vivo antibacterial and antibiofilm activity against carbapenem-resistant Klebsiella pneumoniae. *Microbiology Spectrum.* **12**(8), e03979 (2024).
42. Melchers, R.E. and A.T. Beck, *Structural reliability analysis and prediction*: John wiley & sons. (2018).
43. Rashid, N. N. A. et al. Three-Dimensional structure of human epididymis Protein 4 (HE4): A Protein modelling of an ovarian cancer biomarker through in silico approach: HE4 protein structure modelling and validation. *J. Tropical Life Sci.* **14**(2), 331–348 (2024).
44. Zhou, L. et al. Disulfide-constrained peptide scaffolds enable a robust peptide-therapeutic discovery platform. *PLOS ONE.* **19**(3), e0300135 (2024).
45. Kozakov, D., et al., *The ClusPro web server for protein–protein docking*. **12**(2): p. 255–278. (2017).
46. Alekseenko, A. et al. Protein–protein and protein–peptide docking with ClusPro server. *Protein Structure Prediction*. 157-74 (2020).
47. Lee, M. S. & Kim, Y. J. Signaling pathways downstream of pattern-recognition receptors and their cross talk. *Annu. Rev. Biochem.* **76**(1), 447–480 (2007).
48. Fitzgerald K A, Kagan J C. Toll-like receptors and the control of immunity. **180**(6): 1044-1066 (2020).
49. Mukherjee, S., Huda, S. & Sinha Babu, S. P. Toll-like receptor polymorphism in host immune response to infectious diseases: A review. *Scandinavian J. Immunol.* **90**(1), e12771 (2019).
50. Neyen, C. & Lemaitre, B. Sensing Gram-negative bacteria: a phylogenetic perspective. *Current Opinion Immunol.* **38**, 8–17 (2016).
51. Hornung, V., et al., *RNA recognition via TLR7 and TLR8*. p. 71–86. (2008).
52. Behera, S. K. et al. In Silico Analysis determining the binding interactions of NAD (P) H: Quinone Oxidoreductase 1 and Resveratrol via docking and molecular dynamic simulations. *European Journal of Biology.* **82**(2), 280–288 (2023).
53. Zhu, X. et al. Design of multi-epitope vaccine against porcine rotavirus using computational biology and molecular dynamics simulation approaches. *Virol. J.* **21**(1), 160 (2024).
54. He, J. et al. Evaluation of BVDV E2 proteins based on recombinant baculovirus expression system production as diagnostic antigens and immunogens. *Protein Expr. Purif.* 226(2024).
55. Hofacker, I. L. Vienna RNA secondary structure server. *Nucleic acids Res.* **31**(13), 3429–3431 (2003).
56. Salauddin, M. et al. Development of membrane protein-based vaccine against lumpy skin disease virus (LSDV) using immunoinformatic tools. *Veterinary Med. Sci.* **10**(3), e1438 (2024).
57. Khan, M. F. et al. Exploring optimal drug targets through subtractive proteomics analysis and pangenomic insights for tailored drug design in tuberculosis. *Sci. Rep.* **14**(1), 10904 (2024).
58. Zielkiewicz, J., Structural properties of water: Comparison of the SPC, SPCE, TIP4P, and TIP5P models of water. **123**(10): (2005).

59. Rehman, H. M. et al. Identification of NS2B-NS3 protease inhibitors for therapeutic application in ZIKV Infection: A pharmacophore-based high-throughput virtual screening and md simulations approaches. *Vaccines.* **11**(1), 131 (2023).
60. Kubitzki, M.B., B.L. de Groot, and D. Seeliger, *Protein DynamicsProtein Dynamics: From Structure to Function*, in *From Protein Structure to Function with Bioinformatics*, D. J. Rigden, Editor. 2017, Springer Netherlands: Dordrecht. p. 393-425.
61. McGibbon, R. T. et al. MDTraj: A Modern open library for the analysis of molecular dynamics trajectories. *Biophys. J.* **109**(8), 1528–1532 (2015).
62. Rafiq, H. et al. Evaluation of cannabis-derived anti-inflammatory and analgesic treatment in animals and identification of cannabinoid-based effective inhibition of prostaglandin through computational studies. *J. Biomol. Structure Dynamics* https://doi.org/10.1080/07391102.2025.2472180 (2025).
63. Kumari, R., Kumar, R. & Lynn, A. g_mmpbsa—A GROMACS Tool for High-Throughput MM-PBSA Calculations. *J. Chem. Inf. Model.* **54**(7), 1951–1962 (2014).
64. Yekeen, A. A. et al. CHAPERONg: A tool for automated GROMACS-based molecular dynamics simulations and trajectory analyses. *Comput. Struct. Biotechnol. J.* **21**, 4849–4858 (2023).
65. Fenwick, R. B. et al. Correlated motions are a fundamental property of β-sheets. *Nat. Commun.* **5**(1), 4070 (2014).
66. Yu, H. and P.A. Dalby, *Chapter Two - A beginner's guide to molecular dynamics simulations and the identification of cross-correlation networks for enzyme engineering*, in *Methods in Enzymology*, D.S. Tawfik, Editor. Academic Press.15–49. (2020).
67. Szczyglewska, P., Feliczak-Guzik, A. & Nowak, I. J. M. Nanotechnology–general aspects: A chemical reduction approach to the synthesis of nanoparticles. *Molecules* **28**(13), 4932 (2023).
68. Pronk, S. et al. GROMACS: A high-throughput and highly parallel open source molecular simulation toolkit. *Bioinformatics.* **29**(7), 845–854 (2013).
69. Vaduganathan, M. et al. Effects of canagliflozin on total heart failure events across the kidney function spectrum: Participant-level pooled analysis from the CANVAS Program and CREDENCE trial. *Eur. J. Heart Fail.* **26**(9), 1967–1975 (2024).
70. Holm K, *" A syndrome so characteristic" Molecular and clinical studies of Fusobacterium necrophorum and Lemierre's syndrome.* (2015).
71. Bista, P.K., *Characterization Of Outer Membrane Proteins And Outer Membrane Vesicles And Comparative Genomics To Identify Vaccine Candidates In Fusobacterium Necrophorum*. Purdue University Graduate School (2022).
72. Basmenj, E.R., et al., *Computational epitope-based vaccine design with bioinformatics approach; a review.* (2025).
73. Swetha, R. G. et al. Multi-Epitope vaccine for monkeypox using pan-genome and reverse vaccinology approaches. *Viruses* **14**(11), 2504 (2022).
74. Rafi, M. O. et al. A subunit vaccine against pneumonia: targeting S treptococcus pneumoniae and Klebsiella pneumoniae. *Netw. Model. Anal. Health Inform. Bioinform.* **12**(1), 21 (2023).
75. Werling, D. & Jungi, T. W. TOLL-like receptors linking innate and adaptive immune response. *Vet. Immunol. Immunopathol.* **91**(1), 1–12 (2003).
76. Priyamvada, P. & Ramaiah, S. Pan-genome and reverse vaccinology approaches to design multi-epitope vaccine against Epstein-Barr virus associated with colorectal cancer. *Immunol. Res.* **71**(6), 887–908 (2023).
77. Priyamvada, P. et al. Immunoinformatics strategy for designing a multi-epitope chimeric vaccine to combat Neisseria gonorrhoeae. *Vacunas* **25**(3), 385–402 (2024).
78. Roy, A. et al. Integrating pan-genome and reverse vaccinology to design multi-epitope vaccine against Herpes simplex virus type-1. *3 Biotech.* **14**(7), 176 (2024).
79. Biswas, R. et al. Designing multi-epitope vaccine against human cytomegalovirus integrating pan-genome and reverse vaccinology pipelines. *Biologicals* **87**, 101782 (2024).

Acknowledgements

The authors are thankful to Princess Nourah bint Abdulrahman University Researchers Supporting Project number (PNURSP2025R890), Princess Nourah bint Abdulrahman University, Riyadh, Saudi Arabia.

Author contributions

Conceptualization, Muhammad Naveed; methodology, Muhammad Toheed; software, Muhammad Asim; validation, Maher S. Alwethaynani; formal analysis, Parveen Qadir, investigation, Rania Ali El Hadi Mohamed; resources, Hafiz Muzzammel Rehman; data curation, Fakhria A. Al-Joufi.; writing—original draft preparation, Muhammad Toheed.; writing—review and editing, Tariq Aziz; visualization, Deema Fallatah; Supervision, Tariq Aziz and Muhammad Naveed; project administration, Tariq Aziz.

Declarations

Competing interests

The authors declare no competing interests.

Additional information

Correspondence and requests for materials should be addressed to M.N. or T.A.